University of Stuttgart
Institute of Geodesy

Generating water level time series from satellite altimetry measurements for inland applications

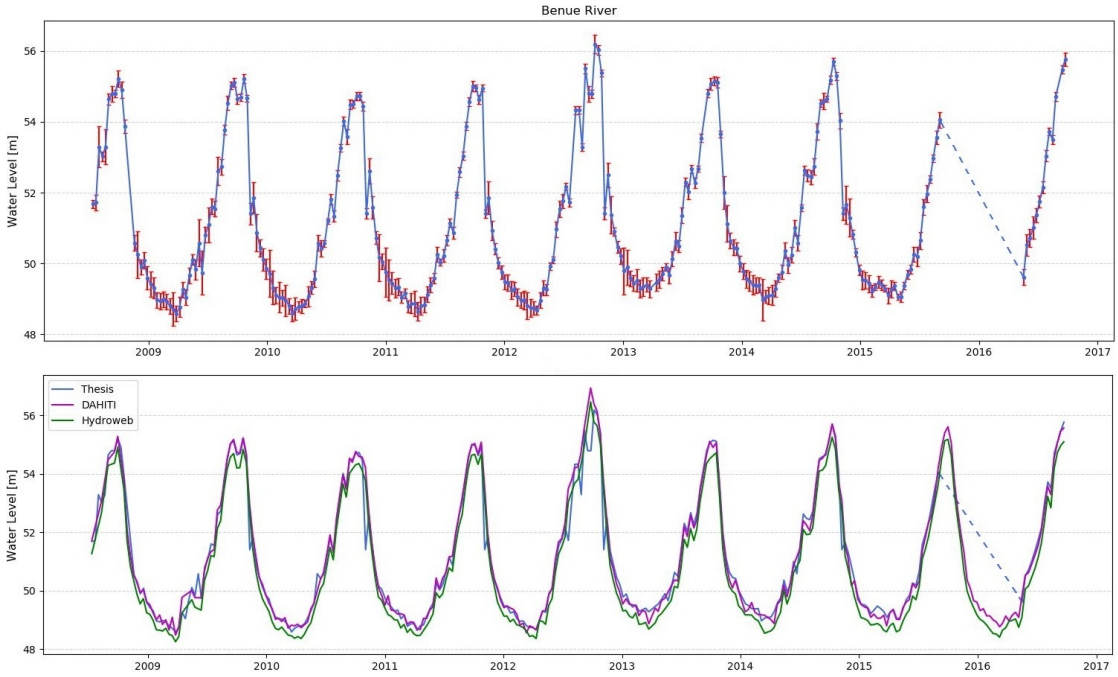

Master Thesis

Geomatics Engineering

University of Stuttgart

Daixin Zhao

Stuttgart, June 2018

Supervisors: M.Sc. Omid Elmi
Prof. Dr.-Ing. Nico Sneeuw
University of Stuttgart

Erklärung der Urheberschaft

Ich erkläre hiermit an Eides statt, dass ich die vorliegende Arbeit ohne Hilfe Dritter und ohne Benutzung anderer als der angegebenen Hilfsmittel angefertigt habe; die aus fremden Quellen direkt oder indirekt übernommenen Gedanken sind als solche kenntlich gemacht. Die Arbeit wurde bisher in gleicher oder ähnlicher Form in keiner anderen Prüfungsbehörde vorgelegt und auch noch nicht veröffentlicht.

Ort, Datum Unterschrift

Abstract

Inland surface water bodies, e.g. lakes and rivers, play vital roles in the nature and in the society. To understand the impact of the human activities and climate change on these vulnerable water resources, monitoring the water level variations with a finer spatial and temporal resolutions is a primary issue. On the other hand, the global available and free accessible in-situ gauge databases are unsatisfactory and insufficient. The spatial distribution of gauge stations is severely uneven and the data accuracy is highly dependent on processing method. Therefore, it is an essential requisite to have a constantly and reliable data stream. Over the past two decades, satellite altimetry has shown the capability to provide repeatable monitoring results for hydrologic cycle and inland water bodies. Several researches and studies are carried out with respect to the improvements on multi-mission data fusion, retracking methods, error estimation and outliers rejection.

In this thesis, we take advantage of this state-of-art inland surface water level monitoring technique to generate the water level time series over Amazon River, Benue River and Tsimlyansk Reservoir. Initially, we investigate the measurement principle, corrections and retracking algorithms of radar altimeter throughly. Afterwards, the processing scheme for water level time series is divided into three steps: data selection, correction and result generation. In this thesis, we have chosen Jason-2 measurement data and the on-board Ice retracker. A validation has been performed between our results and the time series from other databases, e.g. DAHITI and Hydroweb.

The comparisons showed a feasible and acceptable outcomes regarding to correlation coefficient and root-mean-square error (RMSE). The best result was given by Benue River case with 0.98 and 0.96 of correlation coefficient against DAHITI and Hydroweb, respectively. Also, the minimum RMSE difference, $17.1\,\mathrm{cm}$, was achieved between our time series and the one from DAHITI. We also examined the potential error sources when encountering disagreements with others. Furthermore, possible solutions for error elimination and further improvements were also discussed in experiments and outlook.

Contents

List of Figures

List of Tables

List of Abbreviations

AMR	**A**dvanced **M**icrowave **R**adiometer
CLS	**C**ollecte **L**ocalisation **S**atellites
CNES	**C**entre **N**ational d**é**'tudes **S**patiales
DAHITI	**Da**tabase for **H**ydrologi**i**cal **T**ime Series of **I**nland Waters
DC	**D**irect **C**urrent
DORIS	**D**oppler **O**rbitography and **R**adiopositioning **I**ntegrated by **S**atellite
DTC	**D**ry **T**ropospheric **C**orrection
ECMWF	**E**uropean **C**entre for **M**edium-Range **W**eather **F**orecasts
EGM	**E**arth **G**ravitational **M**odel
EMB	**E**lectro**m**agnetic **B**ias
Envisat	**Envi**ronment **Sat**ellite
ERS	**E**uropean **R**espiratory **S**ociety
ESTEC	**E**uropean **S**pace Research and **Te**chnology **C**entre
ET	**E**arth **T**ide
FSSR	**F**lat **S**ea **S**urface **R**esponse
GDR	**G**eophysical **D**ata **R**ecords
GIM	**G**lobal **I**onosphere **M**aps
GPS	**G**lobal **P**ositioning **S**ystem
GRDC	**G**lobal **R**unoff **D**ata **C**entre
IB	**I**nverse **B**arometer
InSAR	**In**terferometric **S**ynthetic-**a**perture **R**adar
JPL	**J**et **P**ropulsion **L**aboratory
LEP	**L**eading **E**dge **P**osition
MWR	**M**icro**w**ave **R**adiometers
NOAA	**N**ational **O**ceanic and **A**tomospheric **A**dministration
OCOG	**O**ffset **C**enter **O**f **G**ravity
OSTM	**O**cean **S**urface **T**opography **M**ission
OT	**O**cean **T**ide
PDF	**P**robability **D**ensity **F**unction
PRF	**P**uls **R**epetition **F**requency
PT	**P**ole **T**ide
PTR	**P**oint **T**arget **R**esponse
RA	**R**adar **A**ltimeter
RMS	**R**oot **M**ean **S**quare
RMSE	**R**oot **M**ean **S**quare **E**rror

SAMOSA	physical **S**AR **Altimetry MO**de **S**tudies and **A**pplications
SAR	**S**ynthetic-**a**perture **R**adar
SARAL	**S**atellite with **AR**gos and **AL**tiKa
SD	**S**tandard **D**eviation
SSB	**S**ea **S**tate **B**ias
SSH	**S**ea **S**urface **H**eight
SWH	**S**ignificant **W**ave **H**eight
TB	**T**racker **B**ias
TEC	**T**otal **E**lectron **C**ontent
TECU	**T**otal **E**lectron **C**ontent **U**nits
VS	**V**irtual **S**tation
WTC	**W**et **T**ropospheric **C**orrection

Chapter 1

Introduction

Water is the basis of life and the most precious natural resource on the Earth. It is not only a prime need for human being, but also plays a vital role in industrial and economic fields. Almost 71 percent of Earth's surface is covered by water. However, only 3 percent out of this is fresh water and 2.5 percent is locked up in ice and glaciers. Hence, people have to rely on 0.5 percent fresh water available for all their needs (Kashid and Pardeshi, 2014).

Inland surface water bodies are an essential component of th hydrologic cycle. Related studies are more concerned about the effects of population growth, over exploitation and toxic waste disposal (Abbott et al., 1986). Many human activities, such as hydroelectricity, irrigation, deforestation and industrialization, lead to a more fragile hydrologic cycle when mismanaged. These activities have a significant impact on the quality, quantity and distribution of inland water bodies, which could be a potential threat for ecosystem and human beings. Furthermore, the rapid change of climate and global warming in recent decades are destroying and altering hydrologic cycle dramatically. Therefore, monitoring and analyzing water level variations with precise measurement data are of great concern.

For the purpose of water resources management and assessments of water vulnerability, one fundamental knowledge is the spatial and temporal behaviors of water resources distribution. Limited measurements of inland water bodies are mostly depend on in-situ networks of gauges that record water surface elevations at fixed locations in rivers and lakes. However, the spatial distribution of gauge stations is severely uneven. The implementation of in-situ gauge networks vary from region to region, and data availability relies on the national policy. Establishment and maintenance of these networks in remote area is difficult and expensive. In addition, measurements accuracy is highly dependent on the processing method and the current status of water bodies. Especially, gauge stations are vulnerable during flood seasons and other extreme circumstances (Biancamaria et al., 2010). Moreover, where and when in-situ gauge time series are accessible, they still suffer from the gaps in recording data, disunity in processing and quality regulation (Harvey and Grabs, 2003). Statistically speaking, a widespread decrease of hydrologic monitoring networks are reported over the last 10-15 years. The

total number of gauges and density of discharge networks declined enormously, which result in the total area monitored decreased by 67 percent from 1986 through 1999 (Shiklomanov et al., 2011). Figure 1.1 demonstrates the spatial distribution and inadequate monitoring capacity of hydrologic gauges around the world. Due to scarcity of accurate measurements and inadequate in-situ gauge stations, accessible and repeatable approach is an essential requisite for monitoring water level variations of inland water bodies.

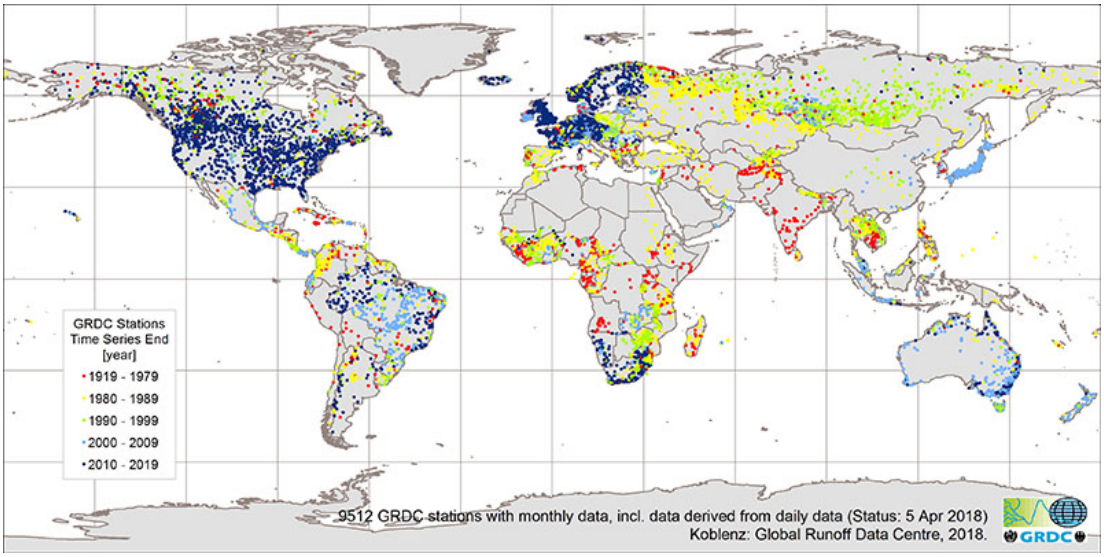

Figure 1.1: *World distribution of water monitoring capacity (GRDC, 2018)*

1.1 Monitoring of water cycle by satellite altimetry

Over the past two decades, thanks to the advances in radar systems and data processing methodology, satellite altimetry has been utilized as a repeatable monitoring tool for hydrologic cycle and inland water bodies (Crétaux and Birkett, 2006). The fundamental principle of satellite altimetry is to measure the distance from satellite itself to the water surface. The radar altimeters on board transmit signals over 1700 pulses per second of microwave radiation with known power towards the Earth and receive the echoes from the target surface, known as the waveform (Chelton et al., 2001). Radar altimeters sample the Earth's surface day and night in all-weather conditions and address a wide variety of hydrologic questions from sea level variation, ocean monitoring, climate change to monitoring water level variations (Stefano Vignudelli and Benveniste, 2011).

Although satellite radar altimeter was initially designed for monitoring oceans, forty years of altimetry missions provide a chance for hydrologic studies in continental-domain as well (Calmant and Seyler, 2006). It can systematically monitor the annual

and interannual variations of water level. Nowadays, there is an increasingly demand for altimeteric observations over the small inland water bodies, e.g. narrow rivers and small lakes. Several studies have been performed, initial work over a few number of targets utilizing Seasat data (Rapley et al., 1987) are followed by more time series extraction from TOPEX/Poseidion mission (Berry et al., 2005; Cazenave et al., 1997; Koblinsky et al., 1993). Also, there has been significant improvement since the launching of the first satellite altimeter. Figure 1.2 shows the accuracy evolution of different altimeter missions since 1978.

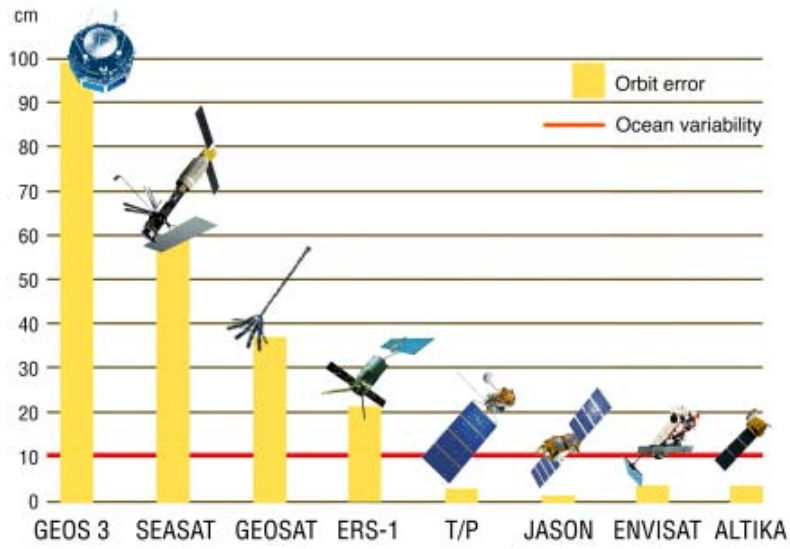

Figure 1.2: *Accuracy evolution of different altimeter missions (CNES and CLS, 2014)*

Satellite altimetry have been proven its excellent performance with accuracy of a few centimeters over oceans, large seas and lakes. With the aid of dense gauge network in the Amazon basin, Birkett et al. (2002) obtained an extensive validation experiment of water levels derived from TOPEX/Poseidon on-board altimeter for seven years. Comparisons with in-situ time series exposed that the derived water level have a mean RMS (Root Mean Square) of $1.1\,\mathrm{m}$. Maheu et al. (2003) examined the water level using TOPEX/Poseidon satellite altimetry data over Plata basin in South America. They achieved the RMS for high and low water seasons with $7\,\mathrm{cm}$ and $24\,\mathrm{cm}$, respectively. Frappart et al. (2006a) constructed water level time series over the lower Mekong River basin using data from TOPEX/Poseidon, ERS-2 and Envisat satellites. The RMS difference between in-situ and derived water levels were $23\,\mathrm{cm}$ at Moc Hoa and $15\,\mathrm{cm}$ at Kg Luong. Frappart et al. (2006b) presented assessment of water levels which derived from Envisat altimeter data over the Amazon basin with different retrackers operationally applied to RA-2 raw data. The RMS discrepancies between measurements were 10, 9, 11 and $13\,\mathrm{cm}$, and the correlation coefficient were 0.98, 0.98, 0.97 and 0.95, respectively. By means of merging the measurements from Envisat and TOPEX/Poseidon mission data, Calmant et al. (2008) presented the RMS difference between altimetry series and

the in-situ series of $8\,\mathrm{cm}$. Fenoglio-Marc et al. (2015) performed an cross-validation and validation analysis to derive precision at open ocean and coast in the German Bight during 2011 and 2012. They utilized CryoSat-2 SAR mode data and arrived at a RMS of $7\,\mathrm{cm}$ for the sea surface height with respect to in-situ gauge data.

Since the application of satellite radar altimetry has been expanded to monitoring and analyzing inland water bodies, researchers encounter the obstacle of complex terrain within the radar footprints. Over topographic surfaces, especially neighbor small and shallow inland water bodies, radar altimeter's on-board tracking system is unable to maintain the echo waveform at the nominal tracking position in the filter bank. This is due to the rapid range variations and will results in a telemetered ranging error know as tracker offset. Therefore, waveform retracking is used as a non-linear ground processing estimation technique in order to obtain the range to the point of closest approach on the surface (Bao et al., 2009).

During the past years, waveform retracking has been performed in multiple studies over rivers and lakes. The Ob River water level change was investigated by Kouraev et al. (2004) during various phases of the hydrologic regime with TOPEX/Poseidon measurements. They arrived a RMS of 23-$40\,\mathrm{cm}$ for the open water period compared to in-situ gauge data, and during ice-covered period up to 2-$3\,\mathrm{m}$ of RMS was observed. Berry et al. (2007) revealed the effective retrieval of inland water heights using Envisat RA-2 measurements data. They obtained a RMS against Brazilian in-situ gauge station of $30\,\mathrm{cm}$. Guo et al. (2009) analyzed data from TOPEX/Poseidon mission over Hulun Lake in the North China. Their results illustrated that waveform retracking perform quite well in the monitoring of lake level variations. In this study the maximum and minimum RMS compared to in-situ observations were $24.7\,\mathrm{cm}$ and $-9.2\,\mathrm{cm}$. Tseng et al. (2013) investigated ice-covered Qinghai Lake within Qinghai-Tibetan Plateau based on Envisat altimetry radar waveform retracking. They indicated a significant improvement with RMS of $6 \pm 7\,\mathrm{cm}$ and a correlation of 0.98 by applying the proper retracking algorithm. The position of retracking gate was estimated from correlation between the waveform of CryoSat-2 InSAR mode and the generic simulated waveform by Kleinherenbrink et al. (2014). In this study, they found a $30\,\mathrm{cm}$ RMS difference between Jason-2 and Cryosat Level-2 data over Nasser Lake in Egypt. In Dubey et al. (2015) the water level variations over Brahmaputra River was derived using SARAL/Altika satellite data. Performance and accuracy analysis have established that water level can be retrieved with less than $40\,\mathrm{cm}$ RMS.

1.2 Objectives

In this thesis, the water level variations over different water bodies are evaluated. Here, generating water level time series from satellite altimetry measurements for inland applications is our main goal. The main objectives are summarized as follow:

- Select satellite radar altimetry data within the chosen area to generate the initial product of water level time series.
- Apply corrections and analyze different retracking methods.
- Implement the outliers elimination algorithm.
- Generate water level time series product for further comparisons.
- Validate water level with other databases and assess the monitoring ability.

1.3 Outline of the thesis

In this thesis, the aforementioned objectives will be investigated in the following chapters. In the chapter 2, the fundamental knowledge for satellite radar altimetry for monitoring inland water bodies will be described. In chapter 3, we will discuss and investigate different retracking algorithms. The methodology, study areas and datasets will be illustrated in chapter 4. In chapter 5, we process selected altimetry data with the on-board corrections and retrackers to derive water level variations in the study areas. Moreover, we will also discuss the validation and numerical results. Chapter 6 includes the conclusion and outlook of this thesis.

Chapter 2

Satellite altimetry

Over the past two decades, satellite altimetry has been used as a repeatable monitoring tool for inland water bodies (Alsdorf and Lettenmaier, 2003; Berry et al., 2005; Crétaux and Birkett, 2006; Papa et al., 2010). Especially, monitoring water level variations in rivers and lakes became the spotlight since the launch of TOPEX/Poseidon and Envisat missions. In the recent years, estimating river discharge with the help of radar altimeter data also investigated by many researchers (Kouraev et al., 2004; Leon et al., 2006; Getirana and Peters-Lidard, 2013).

In the following, we first explain the measurement principle of satellite altimetry. Then, we introduce the technical details of different altimetry satellite missions and corrections for deriving Sea Surface Height (SSH). We will also investigate the potential challenges during the process stage later in this chapter.

2.1 Measurement principles

2.1.1 Waveform construction

Satellite altimeter emits pulses of electromagnetic energy constantly and propagate in a spherical wavefront. This wavefront illuminates the water surface directly under the satellite around the nadir. The area of interaction between surface and radar pulse grows as the illuminated area extends. Then, the altimeter receives the reflected echo, which varies in intensity over time. And these backscattered echoes will form the leading edge of the waveform. Afterwards, due to the limitation of antenna beam width and fewer appropriate reflected facets, the reflected power starts to decline. This forms the long decay of the trailing edge. Unfortunately, the constructed waveform contains noise come from reflected echoes. For the purpose of reducing noise in waveform, the received echoes from subsequent pulses need to be averaged. This averaged waveform (known as the Brown model) is the time series that recorded by satellite altimeter and contains principally three parts (Brown, 1977) as shows in Figure 2.1: thermal noise, leading edge and trailing edge.

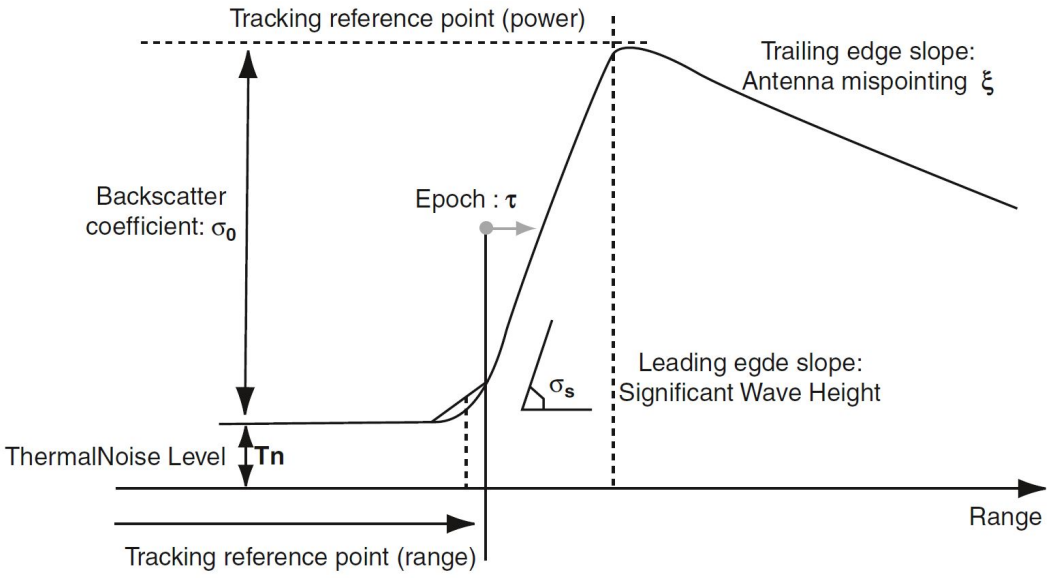

Figure 2.1: *Schematic of a return echo over the ideal water surface (Gommenginger et al., 2011)*

Generally speaking, returned waveform includes the range measurement, the large-scale roughness and the reflectivity of the target surface. The on-board tracker computes the range to the nadir simply by evaluating a two-way travel time of the radar pulse. This travel time represents the time that the mid-point of the radar pulse needs to return from target surface at nadir. Hence, the tracker calculates the time by finding the mid-point (τ in Figure 2.1) on the leading edge and continuously adjusts the range window to keep the leading edge of waveform stable at the fixed center of the range window, known as tracking point (Deng, 2003). The tracking point is a pre-designed parameter for different satellite missions, e.g. 24.5 range bins for TOPEX/Poseidon and 32.5 range bins for Envisat. Therefore, tracker itself will investigate the half-power point on the leading edge and determine the offset to the tracking point (Dudley B. Chelton and Haines, 2001).

On-board tracker could easily identify the half-power point on the leading edge of an ideal waveform. Where the sea surface is flat, as shows in Figure 2.2a, the backscattered wave's amplitude increases sharply from the moment the leading edge of the radar signal strikes the water surface. In rough seas or sea swell, as shows in Figure 2.2b, the echo strikes the crest of one wave and a series of other crests cause the backscattered wave's amplitude to increase constantly. However, the waveforms over inland water bodies do not perform as ideal Brown model. Due to the limited computational time on-board, errors in estimation algorithms and the rapid changes of surface topography, the chances are that these waveforms will show noisy leading and trailing edge, which result in the false range estimations.

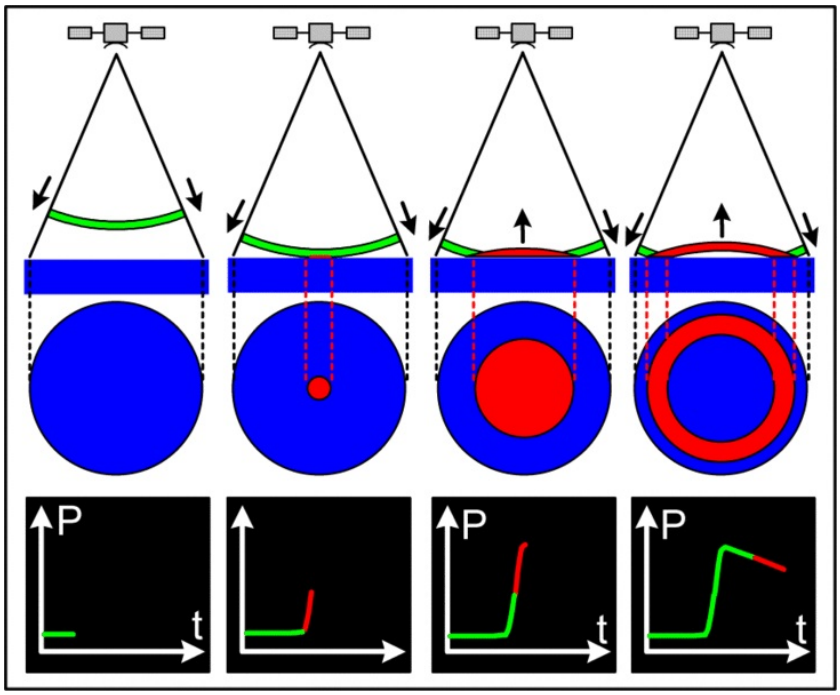

(a) *Reflected waveform for flat sea surface*

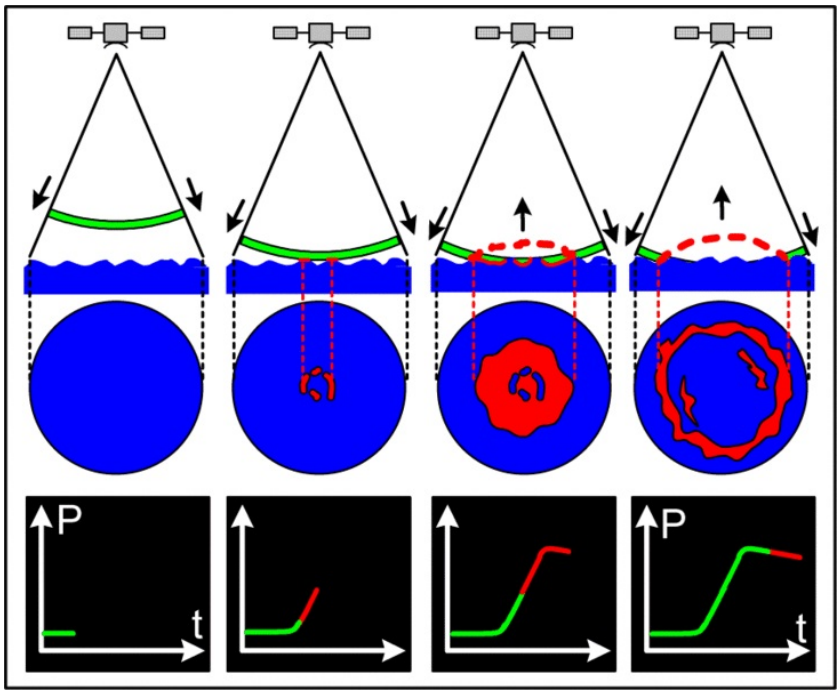

(b) *Reflected waveform for rough sea surface*

Figure 2.2: *Radar altimeter received waveform variation over flat and rough sea surface (AVISO, 2016)*

2.1.2 Footprint size and location

The ground footprint size and location are essential concepts to get the intuition of measurement capability of satellite altimeters. As discussed in the previous part, the projection of the radar pulse onto the water surface contains of a disk area with radius

that grows as the square root of time after leading edge begins to illuminate wave crests at nadir. The radar pulses illuminate a circle of water or land surface with a 3 to 5 wide, which dependent on the wave height, sea state or the crumpled land. Although the water surface is not consistently illuminated within the pulse-limited area, return signals are collected by the satellite altimeter from specular reflectors scattered over the full area of this expanding footprint.

Nevertheless, when altimeter transmits bursts of pulses every ca. $50\,\mathrm{ms}$ and the received waveforms are averaged individually to reduce the measurement noise, the shape of footprint is no longer circular. For the oceanographic applications, the altimeter data is further averaged over about $1\,\mathrm{s}$. The along-track motion of satellite over $1\,\mathrm{s}$ is 5.9 and $6.6\,\mathrm{km}$ for orbit height of 1336 and $785\,\mathrm{km}$, and the along-track dimension of the footprint is around $8.5\,\mathrm{km}$ for flat water surface (Figure 2.3) (Dudley B. Chelton and Haines, 2001). The center of the oval footprint is defined at the subsatellite point along the ground track. Figure 2.4a indicates the oval footprints and subsatellite points of TOPEX/Poseidon's ground track 094 over Balaton Lake.

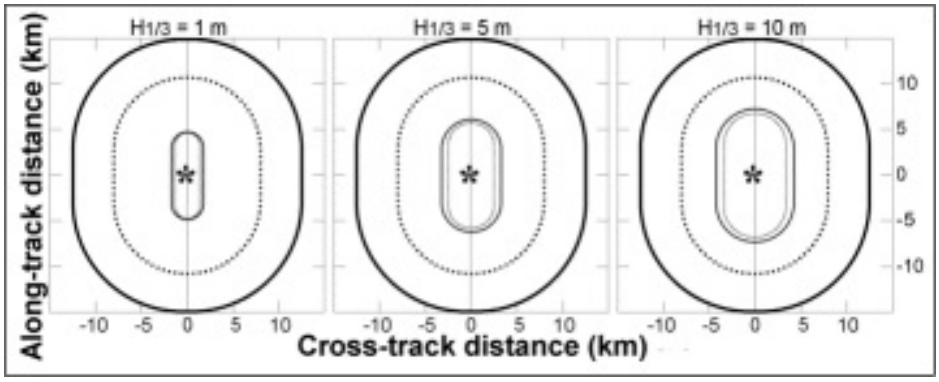

Figure 2.3: *Oval footprint characteristics for Significant Wave Height (SWH) of* 1, 5 *and* $10\,\mathrm{m}$ *for* $1\,\mathrm{s}$ *averages of altimeter measurements at nadir mean sea level from ranges of* $1336\,\mathrm{km}$ *(solid lines) and* $785\,\mathrm{km}$ *(dashed lines) (CNES, 2016)*

For a narrow lake like Balaton, given the ca. $7\,\mathrm{km}$ width at the crossing location of satellite, at most two centers of oval footprints in each pass belong to the water body. Normally, the oval footprints cover both water surface and river bank in inland applications, which lead to the noisy waveforms along the track. Therefore, for these situations, a finer resolution of satellite altimetry is needed (Tourian, 2013). Figure 2.4b, 2.4c show the $10\,\mathrm{Hz}$ waveform over water surface and river bank over Balaton Lake. This gives the intuition of the noisy and unpredictable waveform over land surface.

Additionally, as satellite altimetry is a nadir looking instrument, the location of the footprints should be directly under the satellite. However, there is still some ambiguities in the definition of the subsatellite point. One definition is the point that draw a straight

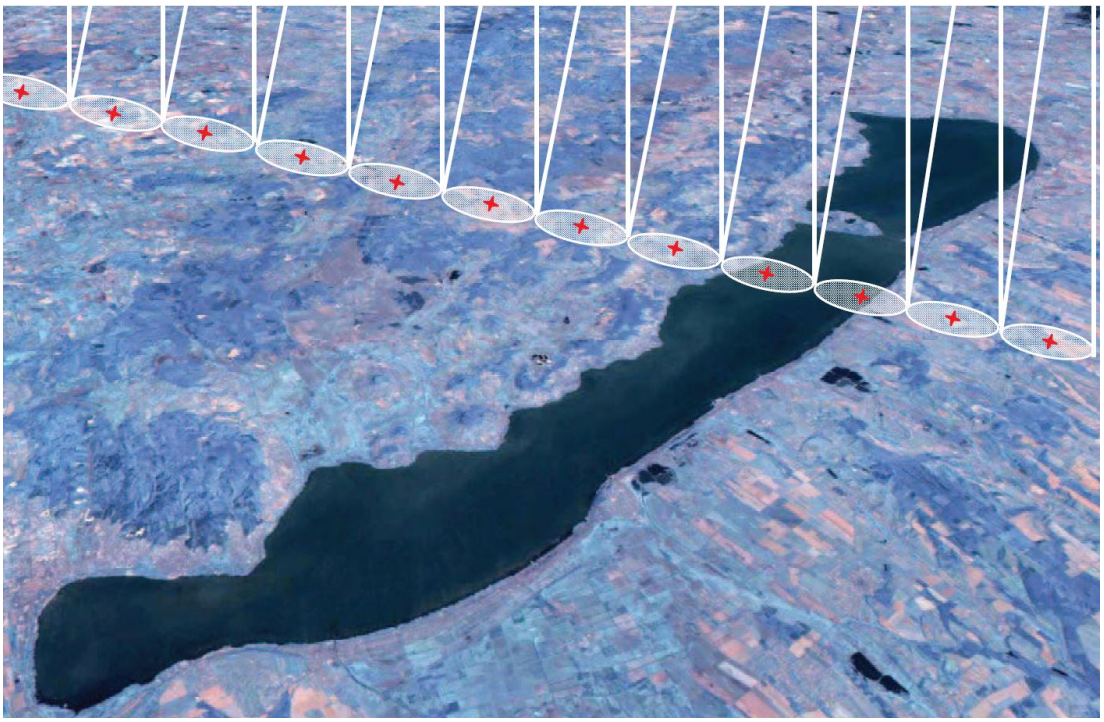

(a) *Schematic oval footprints and subsatellite points over Balaton Lake (Hungary)*

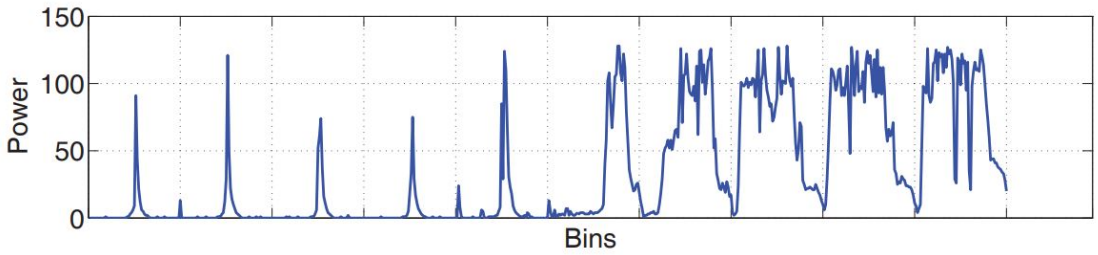

(b) 10 Hz *waveform over Balaton Lake*

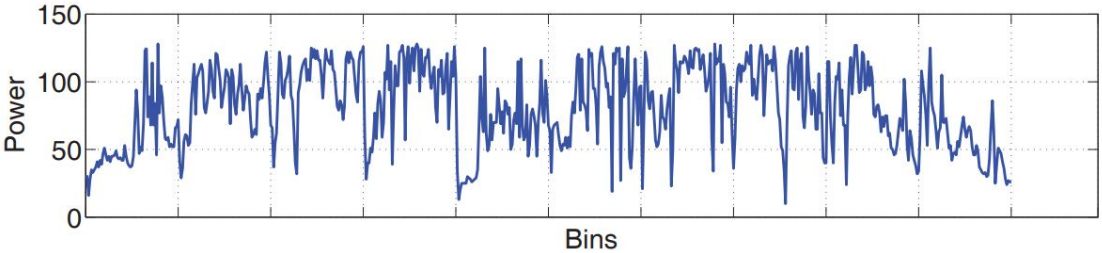

(c) 10 Hz *waveform near Balaton Lake over land*

Figure 2.4: *Schematic oval footprints and subsatellite points over Balaton Lake (Hungary) and TOPEX/Poseidon* 10 Hz *waveform over different areas (Tourian, 2013)*

line connecting the satellite and the Earth centers of mass where intersects with the Earth's surface. A more common definition is the point on the Earth's surface, which defined by the line from satellite center of mass to the local normal to an ellipsoidal approximation of the Earth's surface, known as geodetic subsatellite point. Due to the oblateness of the Earth, the geocentric and geodetic subsatellite points are coincident at the equator and the poles but differ at intermediate latitudes (Dudley B. Chelton and Haines, 2001). The geodetic subsatellite point more nearly represents the measurement location of satellite altimeters.

2.1.3 Range and SSH calculation

The altimeter transmits a short pulse of microwave radiation with known power toward the sea surface and measures the transit time of a radar pulse reflected from the target surface back to itself. If the transit time is measured with a great accuracy, then the distance from the altimeter to the surface can be derived precisely. Figure 2.5 presents the range measurement principle between target water surface and satellite altimeter.

The radar altimeter measurement time t for the pulse to travel round trip between the satellite and the sea surface:

$$t \;=\; 2\,\frac{\hat{R}}{c}\,, \tag{2.1}$$

in which c is speed of light. Hence, the range measurement between altimeter and water surface is determined by:

$$\hat{R} \;=\; \frac{1}{2}\,ct\,. \tag{2.2}$$

The range R from the satellite to mean sea level is estimated from the round-trip travel time and correction parameters:

$$R \;=\; \hat{R} - \sum_{j} \Delta R_j\,, \tag{2.3}$$

in which ΔR_j are corrections of various components including following parameters (NOAA, 2017):

- Inverse barometer correction
- Sea state bias
- Ionospheric correction
- Wet/Dry tropospheric correction
- Pole tide correction

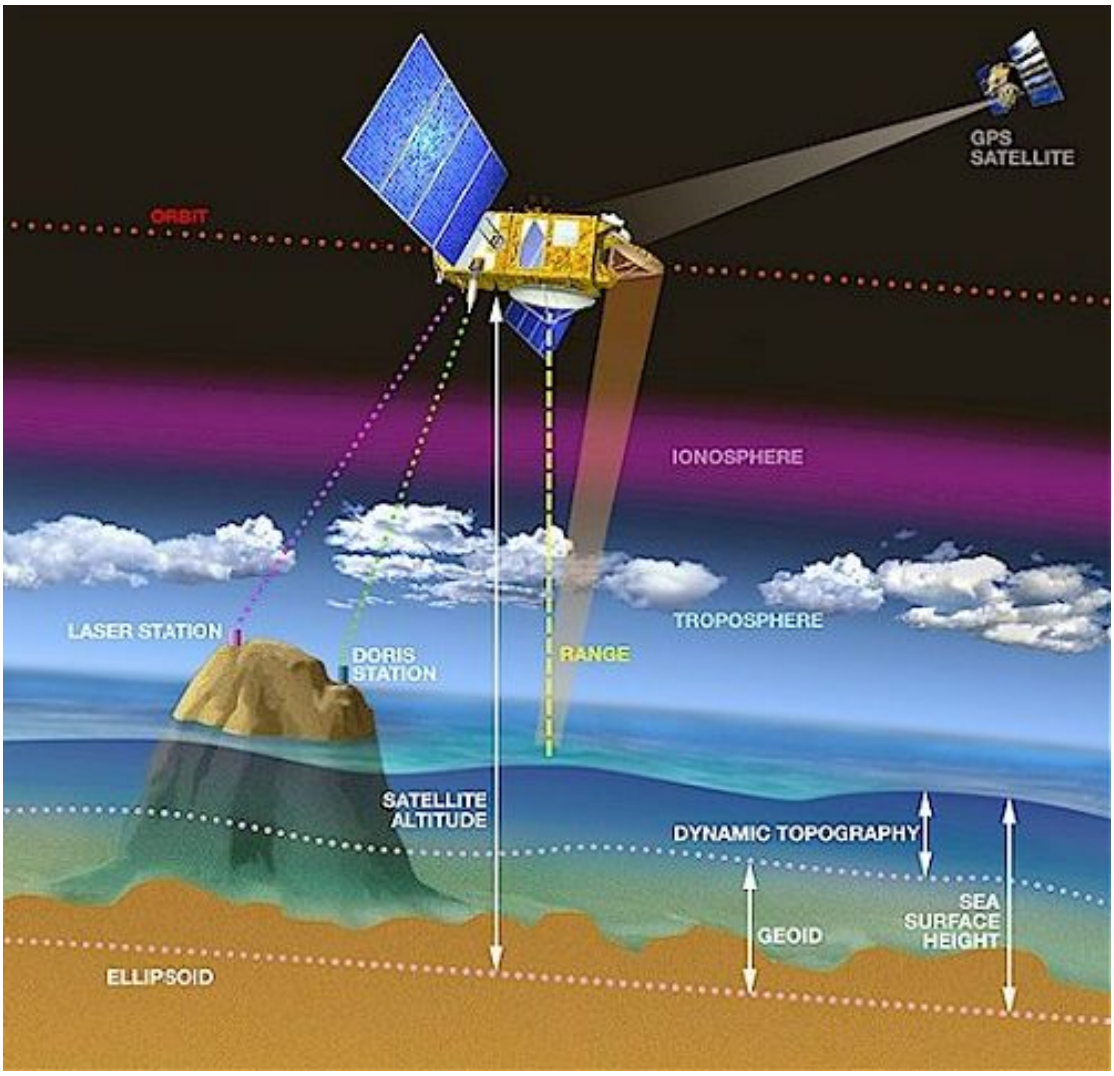

Figure 2.5: *Schematic of satellite altimetry measurement principle (CNES and ESA, 2016)*

- Ocean tide correction
- Earth tide correction
- Reference geoid height

The range estimation equation (2.3) varies along the satellite orbit from both the orbit height relative to the Earth center and the sea surface topography. The precise orbit determination derives the altitude of the altimeter height H above the specified reference ellipsoid approximation of the geoid to centimeter accuracy. The range is then converted to the height h of the sea surface relative to the referenced ellipsoid:

$$\begin{aligned} h &= H - R \\ &= H - \left(\hat{R} - \sum_j \Delta R_j \right) . \end{aligned} \tag{2.4}$$

2.2 Corrections

Altimetric measurements are affected by a considerable amount of errors (Figure 2.6). If the atmosphere were a vacuum, we could easily determine the range from the altimeter to nadir mean sea level from the two-way travel time and the speed of light. However, the existence of dry gases, water vapor and free electrons in the air reduce the transmit speed of radar pulses. Therefore, these additional biases should be considered in the range measurements. It is worth to mention that the range corrections vary both geographically and temporally. We will describe these corrections in the following part.

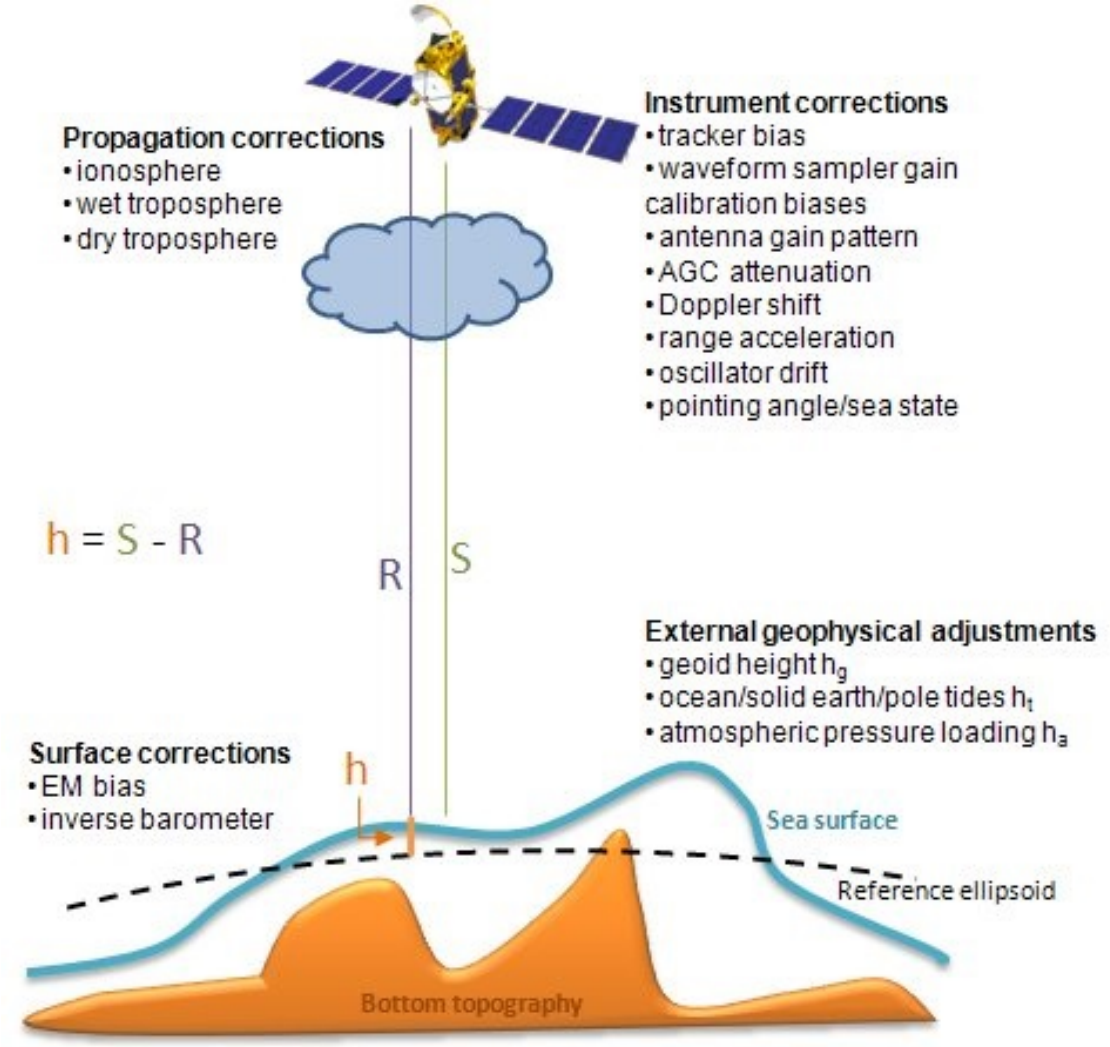

Figure 2.6: *Schematic of geophysical corrections for radar altimetry (http://www.altimetry.info)*

2.2.1 Inverse barometer

The Inverse Barometer (IB) is a static response of the oceans to atmospheric pressure. As the atmospheric pressure increases and decreases, the surface of water bodies tends

to respond hydrostatically, falling or rising respectively. The surface atmospheric pressure also corresponding to the dry tropospheric correction such that a change in dry tropospheric correction also infects the IB correction. Generally, a $1\,\mathrm{mbar}$ increase in atmospheric pressure depresses the sea surface by about $1\,\mathrm{cm}$ (NOAA, 2017).

The instantaneous IB effect on SSH is computed from the surface atmospheric pressure, P_{atm}:

$$\Delta IB \;=\; -9.948 \times (P_{\mathrm{atm}} - P)\,, \tag{2.5}$$

where P_{atm} is the atmospheric pressure and P is the time varying mean of the global surface atmospheric pressure over the oceans.

The scale factor 9.948 is based on the empirical value that indicates the IB response at mid latitudes (Wunsch, 1972). The uncertainty of the atmospheric pressure products on-board TOPEX/Poseidon mission is dependent on location. Typically, errors vary from $1\,\mathrm{mbar}$ in the northern Atlantic Ocean to a few mbars in the southern Pacific Ocean. The translation rate of pressure in error into the IB correction is $1\,\mathrm{mbar}$ to $10\,\mathrm{mm}$.

Notice that mean global pressure over oceans also changed over time. Nowadays we using a static IB correction referenced to a constant mean pressure of $1013.3\,\mathrm{mbar}$ for TOPEX/Poseidon, which gives:

$$\Delta IB_{\mathrm{TOPEX/Poseidon}} \;=\; -9.948 \times (P_{\mathrm{atm}} - 1013.3)\,, \tag{2.6}$$

2.2.2 Sea state bias

The Sea Sate Bias (SSB) is a satellite altimeter ranging error because of the presence of ocean waves and tides on the surface. It refers to the centimeter level range modification applied to correct the range measurement to its corresponding mean sea level (Tran et al., 2010). Accurate SSB correction is critical for ocean applications, it contains Electromagnetic Bias (EMB), Skewness Bias (SB) and Tracker Bias (TB).

The EMB is the difference between the average height of the sea surface specular facet and the average height of the sea level. This is due to wave troughs being better radar reflections than wave crests at nadir. The average scattering level is therefore shifted to the wave troughs concerning the true mean sea level, and the range between the water surface and satellite altimeter is overestimated. In addition, the altimeter range utilizes median instead of the mean reflecting surface in its range estimation. According to the theories and measurements over time, the average height of the specular facet is lower than the mean sea level. This difference is being proportional to the SWH. Typically, values of EMB are between -1% and -4% of SWH (Rodríguez et al., 1992). Thus, the EMB can be expressed as follow:

$$EMB = -(\lambda_2/8)\,\mathrm{SWH}\,, \tag{2.7}$$

in which λ_2 is a function of second- and third-order moments of the joint probability density function of the surface altitude and slope.

Moreover, the median reflecting surface is again lower than the desired mean sea level due to the skewness of the sea height distribution over the satellite footprint arising from strong backscattering of the wave troughs over the wave crest. This gives the SB that described in Scharroo and Lillibridge (2005).

The concept of the TB is defined as the altimeter inherent instrumental and measurement errors associated with range estimation, wave height and backscatter from the returned signals in the tracker's determination of the median height (Dudley B. Chelton and Haines, 2001).

The combination of these three errors give the SSB and it has been proven to be an influential error in the SSH estimation. The error value is mostly between 2% to 5% of the SWH $H_{1/3}$ (Gaspar et al., 1994).

For inland applications, the SSB correction is usually set as approximately zero since the average wave cancels out along-track. Therefore, in small lakes and narrow rivers, SSB correction is negligible. However, over the regions e.g. great lakes, the application of the SSB correction slightly reduces the lake level height anomaly variance at the crossovers.

2.2.3 Ionosphere

As part of the range measurements for satellite altimetry, which enables the water level variations for inland water bodies to be investigated, the refraction that caused by the existence of electrically-charged particles in the atmosphere has to be considered. The majority of those charged particles are exist in the part of atmosphere between the altitude of 50 and $2000\,\mathrm{km}$ called ionosphere, where ions are produced by the photoionization of atomic and molecular gasses (Rush, 1986).

The overall delay affects the radar signal along its path through the ionosphere. Ionospheric correction can be derived from the integral over height of the ionospheric refractivity $N_{\mathrm{ion}}(z)$, which in turn is the proportional to the density of electrons in the ionosphere $n_{\mathrm{e}}(z)$. Besides, the ionospheric refraction also effected by the frequency f by inversely proportional to the square of the frequency (Dudley B. Chelton and

Haines, 2001):

$$\begin{aligned} \Delta\, Ion\,(f) &= 10^{-6}\int_0^R N_{\mathrm{ion}}(z)\,\mathrm{d}z \\ &= \frac{40.3\times 10^6}{f^2}\int_0^R n_{\mathrm{e}}(z)\,\mathrm{d}z\,, \end{aligned} \tag{2.8}$$

where the unit of n_{e} is $\mathrm{electrons/m^3}$, f in Hz and $\Delta\, Ion$ results in meters. The last integral in equation (2.8) represents the atmospheric columnar electron density. This Total Electron Content (TEC) is normally expressed in TECU (TEC Units), with 1 TECU = $10^{16}\mathrm{electrons/m^2}$. Hence, the satellite altimetry ionospheric path delay could be written as:

$$\Delta\, Ion\,(f) = \frac{k\,\mathrm{TEC_{alt}}}{f^2}\,, \tag{2.9}$$

where $k = 0.40250\,\mathrm{m}\cdot\mathrm{GHz}^2\cdot\mathrm{TECU}^{-1}$, f is expressed in GHz, $\mathrm{TEC_{alt}}$ is the total electron content below the satellite altimeter and ΔIon results in meters. For Ku-band (approximately $13.6\,\mathrm{GHz}$) altimeter, this comes out to $2.18\,\mathrm{mm}$ of path delay per TECU (Schreiner et al., 1997). Moreover, the ionospheric effect is frequency dependent and can therefore measured by dual-frequency altimetery mission, e.g. TOPEX, Jason-1, Jason-2 and Envisat. The direct derivation of $\mathrm{TEC_{alt}}$ from the difference between the measured ranges of two frequencies is given as:

$$\mathrm{TEC_{alt}} = \frac{f_{\mathrm{Ku}}^2\, f_{\mathrm{C}}^2}{f_{\mathrm{Ku}}^2 - f_{\mathrm{C}}^2}\,\frac{R_{\mathrm{C}} - R_{\mathrm{Ku}}}{k}\,. \tag{2.10}$$

The ranges R_{Ku} and R_{C} are measured on the Ku-band and C-band ($5.3\,\mathrm{GHz}$ for TOPEX and Jason). The measurements of altimetric heights by both frequencies give an estimate of the ionospheric effect in the envrionment. The correction can also be derived by dual frequency radar systems like GPS and DORIS from models such as those provided Global Ionosphere Maps (GIM). The correction parameter is provided in Jason-2 products.

2.2.4 Dry troposphere

The troposphere delays the altimeter radar pulses at a considerable amount. Dry Troposphere Correction (DTC) is due to the dry neutral gases in the atmosphere and takes into account the path delay in the radar return signal. DTC is the largest range correction in satellite altimetry applications that must be applied to altimeter measurements. With an absolute value about $2.3\,\mathrm{m}$ adjustment and a few centimeter (around $0.2\,\mathrm{m}$) temporal variations, the dry tropospheric range can be approximated by the modified Saastamoinen model (Davis et al., 1985):

$$\Delta DTC = -\frac{0.0022768\,p_{\mathrm{s}}}{1 - 0.00266\cos 2\phi - 0.28\cdot 10^{-6} h_{\mathrm{s}}}\,, \tag{2.11}$$

in which p_{s} is the surface pressure at nadir point in hPa, ϕ is the geodetic latitude, h_{s} is the surface height above the geoid and ΔDTC results in meters. Thus, the dry tropospheric range delay is proportional to sea level pressure and also dependent to the latitude. Since in equation (2.11) p_{s} is the partial pressure of dry air plus water vapor pressure, the expression gives the zenith path delay corresponding to the hydrostatic component of air and not just the dry component of the atmospheric pressure.

The most common source of atmospheric pressure are the atmospheric model from the European Centre of Medium-Range Weather Forecasts (ECMWF). The uncertainty on the ECMWF atmospheric pressure product is dependent on location. Typically, the errors vary from $1\,\mathrm{mbar}$ in the northern Atlantic Ocean to a few mbars in the southern Pacific Ocean. A $1\,\mathrm{mbar}$ error in pressure is corresponding to a $2.3\,\mathrm{mm}$ error in the DTC (NOAA, 2017).

2.2.5 Wet troposphere

The Wet Tropospheric Correction (WTC) is one of the major error sources in altimeter range estimation. This correction is due to the liquid water in the atmosphere which delay the radar return echoes. However, unlike DTC, WTC has a fairly high variability both spatially and temporally. Due to this characteristic, the most accurate method to take this effect into account is to model by the measurements of microwave radiometers (MWR) on-board the satellite altimetry missions.

The passive MWR fetch the water vapor component from the instantaneous measured brightness temperatures near the water vapor absorption line at $22.2356\,\mathrm{GHz}$ (Scharroo et al., 2004). It is important to notice that the algorithms utilized for fetch the WTC assume a constant surface ocean or calm water emissivity. Consequently, when and where satellite is over the surfaces with different emissivity, such as lands, vegetations and even ice covered surfaces, the measurements is to set nullified. Under these circumstances, due to the large footprint of radar altimeter, the MWR measurements over lakes or rivers might be invalid as the radar altimeter footprints emerged lands or vegetations (Desportes et al., 2007; Obligis et al., 2011). Therefore, for inland applications like small lakes and rivers, an alternative sources is essential.

For the usage in satellite altimetric measurements, the WTC can be derived from the total column water vapor (TCWV) and near-surface air temperature T_0 as describe in Bevis et al. (1992):

$$\Delta WTC \;=\; -\left(0.101995 + \frac{1,725.55}{T_{\mathrm{m}}}\right)\frac{\mathrm{TCWV}}{1,000}\,, \tag{2.12}$$

in which T_{m} is the mean temperature of the troposphere. It can be modeled from T_0 as (MENDES, 1999):

$$T_{\mathrm{m}} \;=\; 50.440 + 0.789\,T_0 \tag{2.13}$$

Equation (2.12) and equation (2.13) give the WTC at the level of the atmospheric model orography. On the contrary of DTC, who has a comparably well-know height dependence, the WTC has a large variability. Kouba (2008) had carried out an empirical expression for WTC:

$$\Delta\,WTC(h_{\mathrm{s}}) \;=\; \Delta\,WTC(h_{\mathrm{o}})\,e^{\frac{h_{\mathrm{o}}-h_{\mathrm{s}}}{2000}}\,, \tag{2.14}$$

where h_{s} and h_{o} are the ellipsoidal heights of the model surface and orography. Therefore, the height errors of $1\,\mathrm{cm}$ and $5.6\,\mathrm{cm}$ will lead to a correction of $20\,\mathrm{cm}$.

In Jason-2 products, an improved near land wet path delay algorithm is applied to improve the performance. Also, ECMWF numerical weather prediction model provides a backup when sun glint, anomalous sensor behavior or land contamination.

2.2.6 Pole tide

The Pole Tide (PT) is a tide-like polar motion of the ocean surface that corresponding to the solid Earth and the oceans to the centrifugal potential, which generated by perturbations to the Earth's instantaneous rotation axis (Munk and MacDonald, 1961). The centrifugal potential is temporally determined by periodic alternations in polar motion primarily at the Chandler wobble with a period of 433 days. The displacements of the solid Earth, the body pole tide have amplitudes of up to $10\,\mathrm{mm}$, which dependent on spatially and temporally amplitudes of the Chandler wobble (Wahr, 1985). In the meantime, the displacements of the ocean surface against the ocean bottom, the ocean pole tide, have similar amplitude. Therefore, satellite radar altimeters measure the SSH and contain the sum of body, ocean and load pole tides with amplitudes of up to $20\,\mathrm{mm}$ (Desai, 2002).

The determination of the pole tide requires apply tidal Love numbers to differential centrifugal potential with the potential derived by polar motion observations. The computation of pole tide is described in Wahr (1985) as follow:

$$\Delta PT \;=\; A \cdot \sin 2\phi \cdot [(x - x_{\mathrm{avg}}) \cdot \cos\lambda - (y - y_{\mathrm{avg}}) \cdot \sin\lambda]\,, \tag{2.15}$$

in which ΔPT is expressed in mm, A is the scaled amplitude factor calculated by the Love number in meters. λ and ϕ are the longitude and latitude of the measurement. x and y (in $\mathrm{arc\,second}$) are the nearest previous pole location data relative to the altimeter time as x_{avg} and y_{avg} (in $\mathrm{arc\,second}$) are the averaged pole coordinates.

Nowadays, the time series of perturbations to the Earth's rotation axis is measured consistently with space techniques. The pole tide on the Jason-2 products is computed with a more accurate time series of the Earth's rotation axis and can be directly implemented in various applications.

2.2.7 Ocean tide

The Ocean Tide (OT) refers to the periodic rise and fall of the water surface due to the combined gravitational attraction of the sun and moon. Tides have a strong influence on the modeling of coastal or continental shelf circulations. Since an undisturbed water level is required, the effect of tides must be eliminated from altimetric computed water level heights. The ocean tides are given as the sum of semi-diurnal and diurnal tidal waves measured over the target water surface.

The OT solution based on the GOT00.2 model that has been used for the products in TOPEX/Poseidon mission, can be written as the sum of N tidal constituents h_i (Ray, 1999):

$$\Delta OT = \sum_{i=1}^{N} F_i \cdot [A_i(\phi, \lambda) \cdot \cos \psi_i + B_i(\phi, \lambda) \cdot \sin \psi_i] \,, \tag{2.16}$$

with:

$$\psi_i = \sigma_i \cdot t + X_i + U_i \,. \tag{2.17}$$

Here, σ_i is the tidal frequency. F_i is the tidal coefficient of amplitude nodal correction. X_i is the tidal astronomical value. U_i is the tidal phase nodal correction. F_i, X_i and U_i are dependent only on the altimeter time. In addition, t, ϕ and λ are the altimeter time tag, latitude and longitude, respectively. $A_i(\phi, \lambda)$ and $B_i(\phi, \lambda)$ are harmonic coefficients bilinearly interpolated at the altimeter location (ϕ, λ) from the input harmonic coefficients map given by the GOT00.2b model by Ray (1999). Harmonic coefficients A and B are tidal amplitudes multiply by $\cos(\text{phase})$ and $\sin(\text{phase})$ respectively.

The accuracies of satellite altimetry ocean tide models are significantly dependent on the locations and models themselves (Fok, 2012). The standard deviations of tidal variations in the open ocean are 10-60 cm with even larger values near coastal regions and marginal seas. Due to this negative effect on measurements, the ocean tides can be treated as noise and therefore must be eliminated for estimating the SSH. Recently, satellite altimetry missions can provide the global estimation of tides to an accuracy of 2-3 cm.

2.2.8 Earth tide

The solid Earth responds to the gravitational forces of sun and moon similarly to the oceans. The Earth's response to gravitational forces is fast enough that can be treated in equilibrium with the gravitational forces. The surface is then parallel to the equipotential surface and the derived height is proportional to the potential. The two proportionality constants are the aforementioned Love numbers in section 2.2.6, who are significantly frequency independent (Wahr, 1985).

The Jason-2 products derived solid Earth tide (ET) as a purely radial elastic response of the solid Earth to the tidal potential. The adopted tidal potential is the Cartwright and Tayler (1971) and Cartwright and Edden (1973) tidal potential include degree 2 and 3 coefficients.

2.3 Satellite altimetry missions

Satellite altimetry missions have transformed the way we investigate global water resources. High accurate satellite altimetery measurements provide us a finer resolutions of spatial and temporal over oceans, lakes and rivers even in the remote areas. Figure 2.7 shows different satellite altimetry missions since the first launch back to 1978. Table 2.1 gives the specifications and instrument characteristics for different satellite altimetry missions.

Figure 2.7: *Different satellite altimetry missions (CNES and CLS, 2014)*

Table 2.1: *Specification and instrument characteristics of different altimeter missions (AVISO, 2017)*

Altimeter	Revisit Time	Altitude [km]	Band	Antenna Beamwidth	PRF [Hz]	Waveform Gates	Nominal Tracking Point	Pulse Width [ns]	Gate Width [cm]
SEASAT	17 days	800	Ku	1.59°	1020	60	29.5	3.125	47
GEOSAT	17 days	800	Ku	2.00°	1020	60	30.5	3.125	47
ERS-1	35 days	785	Ku	1.30°	1020	64	32.5	3.030	45
TOPEX	10 days	1336	Ku	1.10°	4500	128	32.5	3.125	47
			C	2.70°	1200	128	32.5	3.125	47
Poseidon	10 days	1336	Ku	1.10°	1700	60	29.5	3.125	47
ERS-2	35 days	785	Ku	1.30°	1020	64	32.5	3.030	45
GFO	17 days	880	Ku	1.60°	1020	128	32.5	3.125	47
Jason-1	10 days	1336	Ku	1.28°	1800	104	31.0	3.125	47
			C	3.40°	300	104	31.0	3.125	47
Envisat	35 days	800	Ku	1.29°	1800	128	46.5	3.125	47
			S	5.50°	450	64	25.5	6.250	94
ICESat-1	90 days	600	Laser	0.029°	40	1000	500	5.000	75
			Laser	0.010°	40	544	272	5.000	75
Jason-2	10 days	1336	Ku	1.26°	1800	104	31.0	3.125	47
			C	3.38°	300	104	31.0	3.125	47
Cryosat-2, SAR	365 days	717	Ku	1.08°, 1.20°	18181	128	63.0	1.5625	23
Cryosat-2, SARIn	365 days	717	Ku	1.08°, 1.20°	18181	512	255.0	1.5625	23
SARAL/Altika	35 days	800	Ka	1.29°	1800	128	46.5	3.125	47
Jason-3	10 days	1336	Ku	1.28°	1800	104	31.0	3.125	47
			C	3.40°	300	104	31.0	3.125	47

2.3.1 OSTM/Jason-2

In this study, Jason-2 satellite altimetry mission is used to investigate and generate the water level time series. Jason-2 takes over and continues TOPEX/Poseidon and Jason-1 missions on June 20, 2008, in the frame of the cooperation between CNES, EUMETSAT, NASA and NOAA. Jason-2 carries the same payload compare to its two predecessors for a high-accuracy sea surface measurement.

The Jason-2 is carrying the Poseidon-3 altimeter, which is the mission's main instrument for range measurement. It emits radar pulses in two frequencies: Ku band operating at $13.6\,\mathrm{GHz}$ and C band operating at $5.3\,\mathrm{GHz}$. The dual-frequency system estimated the two-way travel time very precisely to derive the range after applying corrections. Jason-2 also carries an Advanced Microwave Radiometer (AMR) that measure perturbations due to atmospheric water vapor and liquid water content. It helps satellite altimeter to determine how atmosphere affects the radar signal propagation.

Jason-2's high altitude has weaken the Earth's atmosphere and gravity field interaction to keep a more precise orbit. The orbit inclination of 66° enables the satellite altimeter to cover most of the unfrozen water areas. After the spatial and temporal resolutions trade-off, every 9.9156 days Jason-2 will passes over the same point at Earth's surface. The altimetry measurements data contains satellite position and timing, radar measurements of the range between satellite and reflecting surface, correction parameters and flags. Jason-2 also has on-board altimeter retracking algorithms, such as Ocean retracking and Ice retracking, to give an accurate range estimations.

2.4 Challenges of inland altimetry

2.4.1 Off-nadir effect

As satellite altimeter is a nadir range measuring instrument, the footprint location is supposed to be directly under the altimeter. However, when the altimeter pulses illuminate on the inland water bodies that contains rough terrain and vegetation coverage, the nadir mis-pointing happens very often. This phenomenon occurs especially over small inland water bodies such as narrow rivers and small lakes.

Figure 2.8 shows the off-nadir effect in the along-track water height profiles. In this figure, a_i, $a_{i'}$ and $a_{i''}$ are the satellite altitudes. ρ_i, $\rho_{i'}$ and $\rho_{i''}$ are the off-nadir ranges at the successive times t_i, $t_{i'}$ and $t_{i''}$, respectively. a_o is the satellite altitude and ρ_o is equivalent nadir range at the time of passing at the zenith of the water body. H_o is the true ellipsoidal height of the water body. H_i, $H_{i'}$ and $H_{i''}$ are the heights of the water body obtained by subtracting the off-nadir ranges from the satellite altitudes

at successive times t_i, $t_{i'}$ and $t_{i''}$, respectively. Note that geophysical corrections are omitted in this schematic view (da Silva et al., 2010).

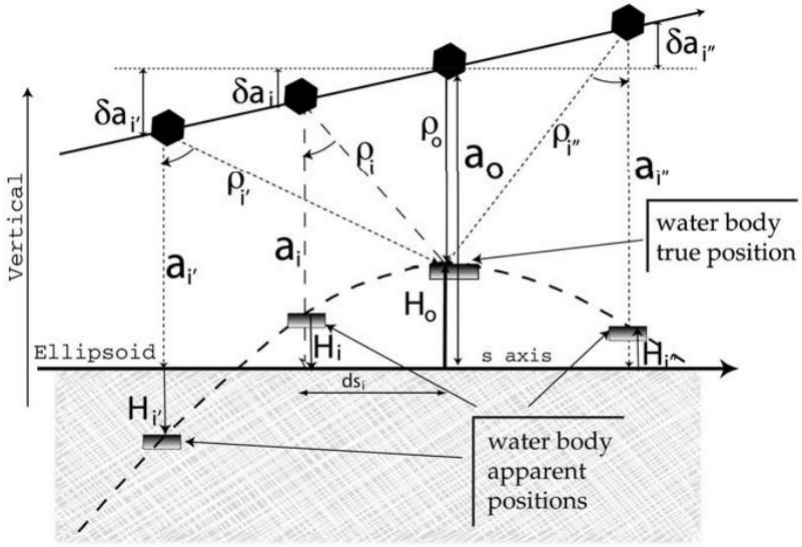

Figure 2.8: *Diagram of the off-nadir effect in along track water height (da Silva et al., 2010)*

Off-nadir effect brings the opportunity to get more data from the water bodies, as the antenna locks over the water area before and after the nadir location. This gives a better estimation of water level variations and time series measurements. However, in small lakes and narrow rivers, off-nadir measurements might result in an erroneous water level time series. For the purpose of generating reliable and accurate time series of selected water bodies, the off-nadir correction and the virtual station location should be investigated.

2.4.2 Insufficient resolution

Since the satellite altimetry missions are firstly designed for the purpose of monitoring global oceanographic variations, it can provide the coverage of 90% of the world's oceans within a few days cycle. However, many of the inland surface water bodies are not sensed by these altimetry missions due to the insufficient spatial and temporal resolutions. Biancamaria et al. (2010) indicated that satellite altimetry missions can only monitor 15% of global water volume variations of the inland water bodies. Thus, there is still a large gap for hydrologic modeling in continental-domain with respect to spatial and temporal resolutions.

Considering the spatial resolution for instance, there are lakes in Figure 2.9 that can be observed neither by TOPEX-series nor Envisat XT. TOPEX-series, such as Jason-1 and Jason-2, is capable to monitoring same areas within a 10-day repeat cycle. But with the

satellite inclination of 66°, there are still a number of inland water bodies can not be detected and monitored. Hence, the spatial resolution is unsatisfactory by this mission.

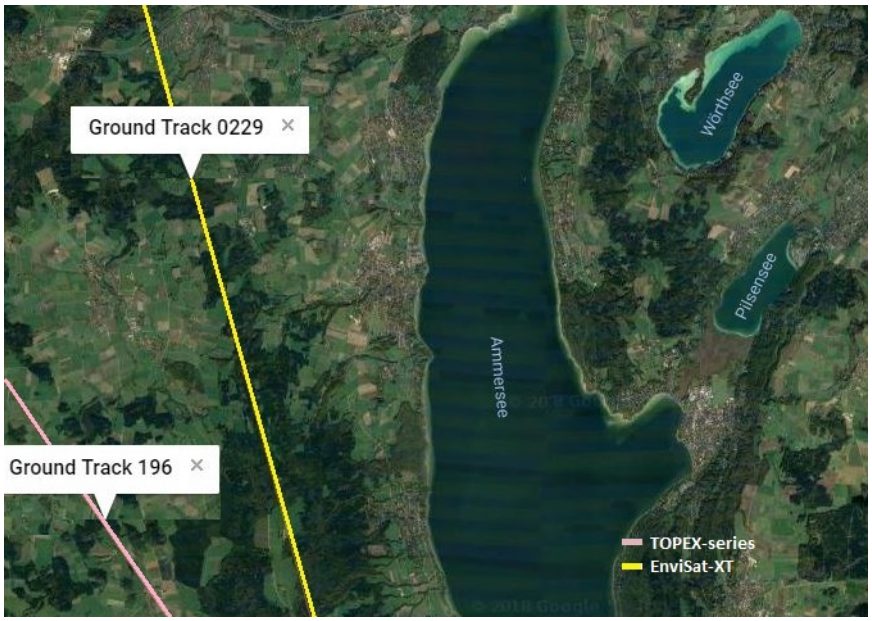

Figure 2.9: *Ammersee, Wörthsee and Pilsensee and neighboring altimetry missions ground track in Bavaria, Germany*

Another obstacle is the temporal resolution due to various orbit design for different satellite altimetry missions. Retrieving the temporal behavior of water level variation is an important task. For example, CryoSat-2 mission can observe surface water bodies with a fairly high spatial resolution, but the revisit time is longer than 365 days (Table 2.1). Therefore, the seasonal or monthly behavior of small lakes and rivers can not be detected.

Moreover, the lifetime of different satellite missions is limited so that we do not have a constantly access to altimetry data for building water level time series. In order to monitoring annual and interannual water level variations at the global scale, researchers have to combine the measurements from different altimetry missions. But the disadvantage of this combination is that, it will bring systematic biases from different radar altimeter instruments.

2.4.3 Noisy waveform

Another challenge of monitoring inland water bodies using satellite altimetry is the response of the altimeter to water bodies and their surrounding topography. Due to the inhomogeneous surface within the large footprints of radar altimeters, the shape of return echoes over narrow rivers and wetlands is multi-peaked or narrowly peaked.

Consequently, the construction of water level time series is noisy and inaccurate. Therefore, waveforms need to be retracked to provide a precise range measurements and derive accurate water level variations. The principle of waveform retracking and several waveform retracking algorithms will be described in the next chapter. Figure 2.10 explains the waveform contamination over inland water bodies schematically.

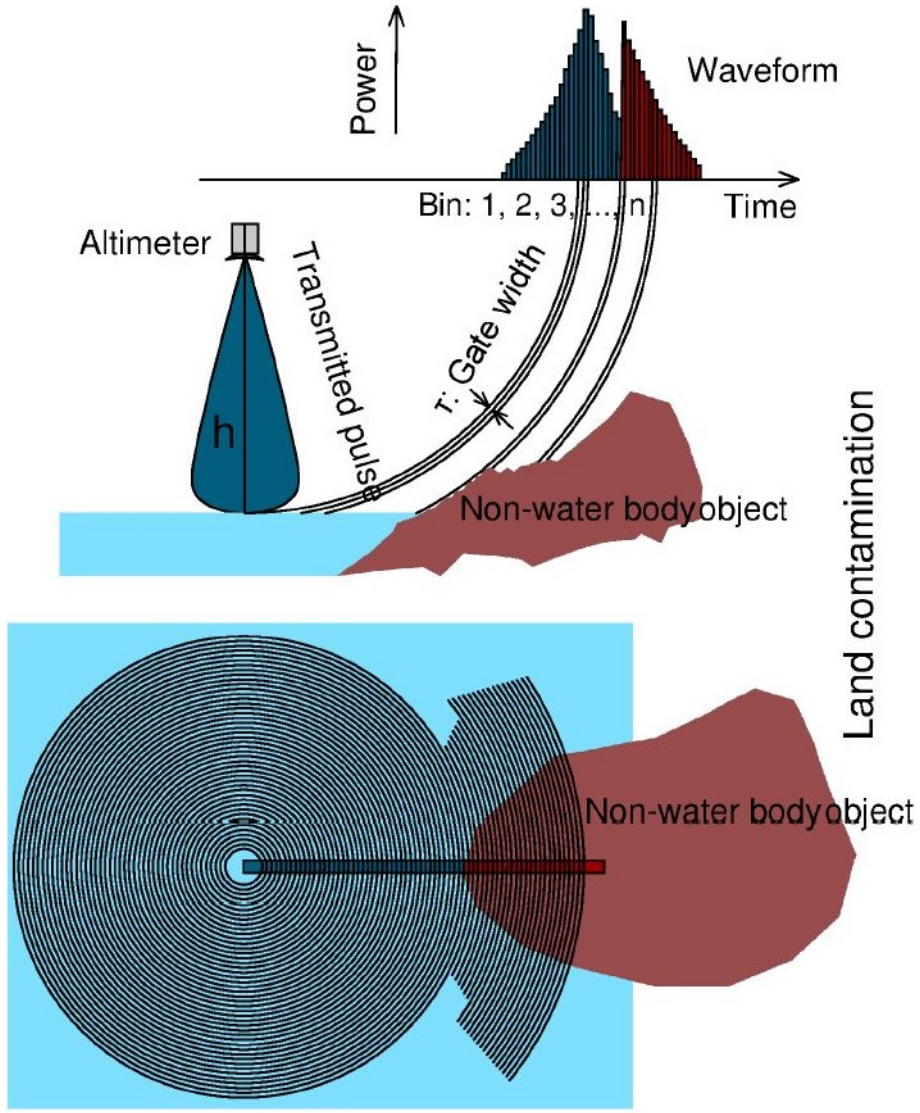

Figure 2.10: *Principle of noisy waveform in the case of water/land transition (Roohi, 2017)*

The top panel of the figure shows how the last samples of the waveform are contaminated by non-water body objects, such as land. Similarly, during a land to water transition, the closer the satellite nadir location is from the land, the more returns from water cells contaminate the last samples of the waveform. The lower panel of the figure is the top-down view of the altimeter footprint corresponding to the surface underneath.

Chapter 3

Waveform retracking

Retracking is a post-processing procedure of radar altimeter waveform data to improve the parameter estimations. The on-board processors use a nominal gate in the waveform as a reference gate for tracking process. For instance, tracking gate of 46.5 for RA-2 on Envisat, gate of 24.5 in a 64-sample waveform for TOPEX/Poseidon and gate of 32 in a 104-sample waveform on-board the Jason-2 (Kouraev et al., 2004). Therefore, the range estimations can be erroneous especially for inland applications. To keep the returned waveforms centered in the tracking window for on-board computer to record the accurate pulse's travel time and derive reliable range estimation, different retracking algorithms are implemented for several altimetry missions (Bao et al., 2009; Guo et al., 2009).

In this chapter, different waveform retracking algorithms will be described in detail. These algorithms can be divided into empirical retrackers, such as threshold retracking, OCOG and β-parameters, and physical retrackers, such as Ice-2 and Ocean retracking (Gommenginger et al., 2011). The retracked range correction is determined as follow:

$$\Delta R_{\mathrm{ret}} \;=\; (Gate_{\mathrm{ret}} - Gate_{\mathrm{nom}})\,\tau\frac{c}{2}\,, \tag{3.1}$$

where $Gate_{\mathrm{ret}}$ is the retracking gate and $Gate_{\mathrm{nom}}$ is nominal tracking gate. The parameter τ is the pulse width included in Table 2.1. The gate or bin is the number of samples in a given waveform.

3.1 Empirical waveform retracking algorithms

3.1.1 Threshold retracker

The threshold retracker was originally developed by Davis (1995) for measuring ice sheet elevations and growth rates. But this retracker and its variations can also applied on coastal and lake areas. For basic threshold retracking, the leading edge of the return waveform is sought by finding the first range bin to exceed a percentage of the maximum waveform amplitude. The pre-leading edge DC bias (mean value of the waveform) is different for various satellites and also corresponding to the location and time

of the given satellite dataset. A 10% or 20% threshold level for volume-scattering surface, 50% threshold for surface-scattering waveform is recommended by Davis (1997).

Let the array of waveform data samples be WD_n, in which n stands for the range gate number. Therefore, the maximum amplitude A_{max} is given by:

$$A_{max} = \max(\mathrm{WD}_n)\,. \tag{3.2}$$

The pre-leading edge DC level is estimated by:

$$\mathrm{DC} = \frac{1}{5}\sum_{n=\tilde{n}}^{\tilde{n}+4}\mathrm{WD}_n\,, \tag{3.3}$$

in which $\tilde{n}$ is the position of the first unaliased waveform sample. Therefore, the threshold level can be written as:

$$\mathrm{Th} = \mathrm{DC} + p(A_{max} - \mathrm{DC})\,, \tag{3.4}$$

where p is the percentage value of the maximum waveform above the DC level. So the retracking gate $Gate_{\mathrm{ret}}$ on the leading edge is defined as:

$$Gate_{\mathrm{ret}} = (\hat{n}-1) + \frac{\mathrm{Th} - \mathrm{WD}_{\hat{n}-1}}{\mathrm{WD}_{\hat{n}} - \mathrm{WD}_{\hat{n}-1}}\,. \tag{3.5}$$

Thus, with the conversion factor q from gates to meters and on-board altimeter tracking gate $Gate_{\mathrm{nom}}$, the final corrected altimeter range measurement is given by:

$$\Delta R_{\mathrm{ret}} = q\,(Gate_{\mathrm{ret}} - Gate_{\mathrm{nom}})\,. \tag{3.6}$$

3.1.2 Offset Center of Gravity (OCOG) retracker

A robust retracking algorithm OCOG was developed by Wingham et al. (1986) based on statistical approach. The algorithm finds the center of graivty (COG) of the waveform based on power levels within the gates. The height of the rectangular box is defined by the double digits of gravity center height, which marked as amplitude A. The width of the box is marked as W. Figure 3.1 shows a schematic description of the OCOG retracker.

Based on the definition of the rectangular box, the following formula is given:

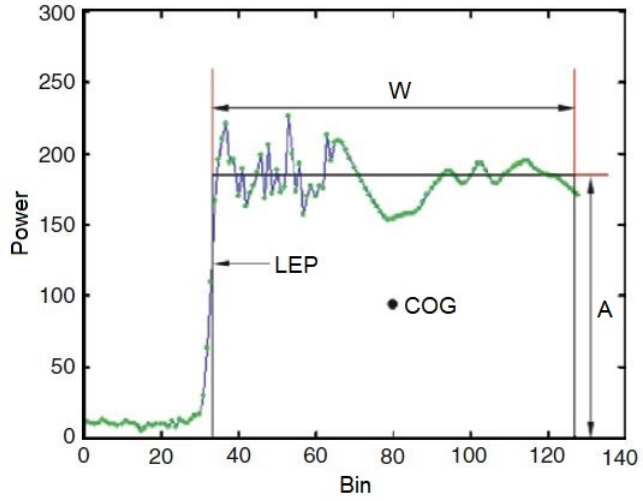

Figure 3.1: *Schematic description of the OCOG retracker (Gommenginger et al., 2011)*

$$COG = \sum_{i=1+n_1}^{N-n_2} iP_i^2(t) \Big/ \sum_{i=1+n_1}^{N-n_2} P_i^2(t)\,, \tag{3.7}$$

$$A = \sqrt{\sum_{i=1+n_1}^{N-n_2} P_i^4(t) \Big/ \sum_{i=1+n_1}^{N-n_2} P_i^2(t)}\,, \tag{3.8}$$

$$W = \left(\sum_{i=1+n_1}^{N-n_2} P_i^2(t)\right)^2 \Big/ \sum_{i=1+n_1}^{N-n_2} P_i^4(t)\,, \tag{3.9}$$

in which P_i is the waveform power at i^{th} bin, N is the total number of samples in the waveform. n_1 and n_2 are the numbers of bins in the waveform, who affected by aliasing at the beginning and the end. The leading edge position (LEP) is:

$$\text{LEP} = Gate_{\text{ret}} = COG - \frac{W}{2}\,. \tag{3.10}$$

OCOG retracker is simple to implement but sensitive to the shape of waveforms due to its independence of surface's physical characteristics. It is usually used as the backbone of other retrackers such as Ice-1 retracker on Envisat, β-parameter retracker and SAMOSA3.

3.1.3 β-parameter retracker

The β-parameter retracker was developed by Martin et al. (1983) to processing altimeter waveforms over continental ice sheets. This retracker uses a relevant parametric function based on Brown model to fit the single or double-ramped waveform. Basically, it comes as a 5-parameter and a 9-parameter functional form.

The 5-parameter retracker is normally used for fit a single-ramp waveforms (Figure 3.2). The general formulas of the 5-parameter retracker are given as:

$$y(t) = \beta_1 + \beta_2(1 + \beta_5 Q)P\left(\frac{t-\beta_3}{\beta_4}\right), \tag{3.11}$$

with:

$$Q = \begin{cases} t - (\beta_3 + 0.5\beta_4) & for \quad t \geq \beta_3 + 0.5\beta_4 \\ 0 & for \quad t < \beta_3 + 0.5\beta_4 \end{cases}, \tag{3.12}$$

$$P(x) = \int_{-\inf}^{x} \frac{1}{\sqrt{2\pi}} \exp\left(\frac{-q^2}{2}\right) \mathrm{d}q\,. \tag{3.13}$$

The unknown parameters β relate to the waveform shape as follow:

- β_1: thermal noise level of the waveform
- β_2: return signal amplitude
- β_3: mid-position of the leading edge
- β_4: waveform rise-time
- β_5: slope of trailing edge

The linear trailing edge can be replaced by the exponential decay term for extend usage (Figure 3.3). The formulas of 9-parameter retracker with exponential trailing edge are given as (Deng and Featherstone, 2006):

$$y(t) = \beta_1 + \sum_{i=1}^{2} \beta_{2i}(1 + \beta_{5i} Q_i)P\left(\frac{t-\beta_{3i}}{\beta_{4i}}\right), \tag{3.14}$$

with:

$$Q = \begin{cases} t - (\beta_{3i} + 0.5\beta_{4i}) & for \quad t \geq \beta_{3i} - 2\beta_{4i} \\ 0 & for \quad t < \beta_3 - 2\beta_4 \end{cases}, \tag{3.15}$$

$$P(x) = \int_{-\inf}^{x} \frac{1}{\sqrt{2\pi}} \exp\left(\frac{-q^2}{2}\right) \mathrm{d}q\,. \tag{3.16}$$

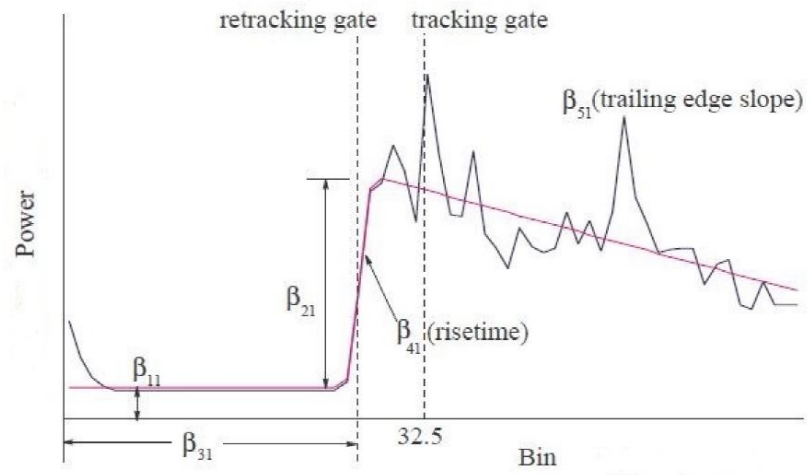

Figure 3.2: *5-parameter retracker fit a single-ramp waveform (Martin et al., 1983)*

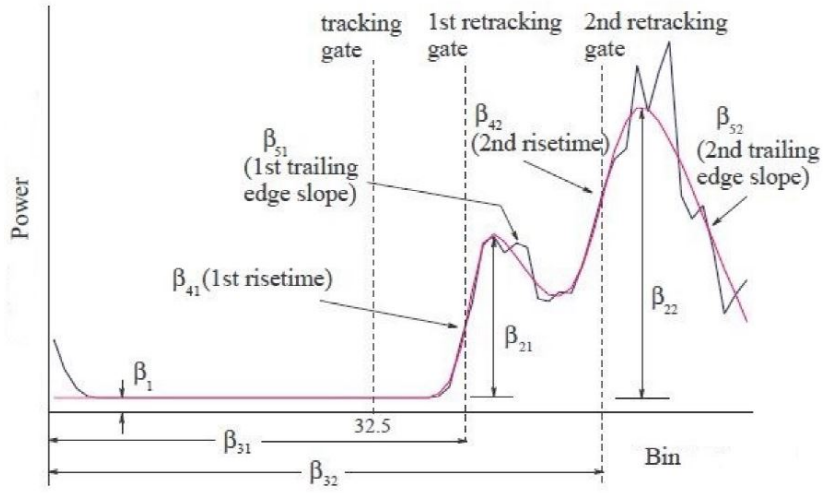

Figure 3.3: *9-parameter retracker fit a double-ramp waveform (Martin et al., 1983)*

Finally, the range corrections can be derived by computing the offset between the mid-position of the leading edge β_3 and nominal tracking gate:

$$\Delta R_{\mathrm{ret}} \;=\; (\beta_3 - Gate_{\mathrm{nom}}) \times \tau \times \frac{c}{2}\,. \tag{3.17}$$

The empirical β-parameters are not related to the physical properties. Both 5-parameter and 9-parameter retracker can use least square method to derive β_1-β_5. The parameter β_5 controls the slope of trailing edge, which can be used to extract the information about radar altimetry mispointing.

3.2 Physically-based waveform retracking algorithms

3.2.1 The Brown-Hayne theoretical ocean model

This physically-based retracker is derived from theoretical knowledge of microwave scattering at nadir. Barrick and Lipa (1985) carried out that for a rough scattering surface, the average return power to the function of time delay t can express convolutionally as follow:

$$W(t) \;=\; FSSR(t) * PTR(t) * PDF(t)\,, \tag{3.18}$$

in which $FSSR$ is the flat sea surface response, PTR is the radar point target response, PDF is the probability density function of ocean surface elevation at specular points. The PTR function is a $(\sin x/x^2)$ function which normally approximated by Gaussian function:

$$PTR(t) \;\approx\; \exp\left(\frac{-t^2}{2\sigma_p^2}\right)\,, \tag{3.19}$$

where $\sigma_p = \dfrac{1}{2\sqrt{2\ln 2}} r_t \approx 0.425\, r_t$, illustrates the width of the radar point target response function, with time resolution r_t. This assumption is used by Hayne (1980) in the refined analytical ocean return model and also be used in the TOPEX-series ground processing.

The formula for the theoretical shape of an echo over the surface include fixed skewness parameter λ_s reads:

$$\begin{aligned} V_m(t) \;=\; & T_n + a_\xi \frac{P_u}{2} \exp(-v) \Bigg\{ [1+\mathrm{erf}(u)] + \frac{\lambda_s}{6}\left(\frac{\sigma_s}{\sigma_c}\right)^2 \Bigg\{ [1+\mathrm{erf}(u)] c_\xi^3 \sigma_c^3 \\ & - \frac{\sqrt{2}}{\sqrt{\pi}} \left[2u^2 + 3\sqrt{2} c_\xi \sigma_c u + 3 c_\xi^2 \sigma_c^2 - 1\right] \exp(-u^2) \Bigg\} \Bigg\}\,, \end{aligned} \tag{3.20}$$

in which:

$$\mathrm{erf} = \left(\frac{2}{\sqrt{\pi}}\right) \cdot \int_0^x e^{-t^2} \mathrm{d}t \qquad \gamma = \frac{\sin^2(\theta_0)}{2\ln(2)}$$

$$a_\epsilon = \exp\left(\frac{-4\sin^2\xi}{\gamma}\right) \qquad b_\xi = \cos(2\xi) - \frac{\sin^2(2\xi)}{\gamma}$$

$$c_\xi = b_\xi a \qquad a = \frac{4c}{\gamma h\left(1 + \dfrac{h}{R_e}\right)}$$

$$u = \frac{t - \tau - c_\xi \sigma_c^2}{\sqrt{2}\sigma_c} \qquad v = c_\xi \left(t - \tau - \frac{c_\xi \sigma_c^2}{2} \right)$$
$$\sigma_c^2 = \sigma_p^2 + \sigma_s^2$$

with the light velocity c, satellite altitude h, Earth radius R_e, off-nadir mispointing angle ξ and antenna beam width θ_0. When the PDF of the ocean surface elevation at specular points is assumed Gaussian, the skewness λ_s in equation (3.22) equals to zero and will reduce regarding to the Brown model.

3.2.2 Ice-2 retracker

The Ice-2 retracker was initially developed to perform retracking the received Ku-band and C-band waveforms over continental ice sheets. The formula of the model with respect to time t is derived from Brown model. According to Legrésy and Remy (1997), least square estimators are used to make the waveform coincides with a return power model:

$$V_m(t) = \frac{P_u}{2} \cdot \left[1 + \mathrm{erf}\left(\frac{t - Gate_\mathrm{ret}}{\sigma_\mathrm{L}} \right) \right] \exp[s_T \cdot (t - Gate_\mathrm{ret})] + P_n \,, \tag{3.21}$$

in which $\mathrm{erf}(x) = \frac{2}{\sqrt{\pi}} \int_0^x e^{-t^2} \mathrm{d}t$, P_n is the thermal noise level to be removed from the waveform samples, σ_L is the width of the leading edge, s_T is the slope of the logarithm of the waveform at the trailing edge, P_u is the amplitude related to the backscatter coefficient.

3.2.3 Ocean retracker

The ocean retracking algorithm is the result for several comparative studies of standard ocean retrackers, i.e. of:

- JPL algorithm for processing TOPEX altimetric data
- CNES/CLS algorithm for processing Poseidon altimetric data
- ESTEC algorithm for processing ERS altimetric data
- ALENIA algorithm for processing Envisat altimetric data

The ocean retracker can be performed on both Ku-band and C-band, the general expression is given by Hayne (1980):

$$V_m(t) = a_\xi \frac{P_u}{2} \exp(-v) \Bigg\{ [1 + \mathrm{erf}(u)] + \frac{\lambda_s}{6} \left(\frac{\sigma_s}{\sigma_c} \right)^2 \Bigg\{ [1 + \mathrm{erf}(u)] c_\xi^3 \sigma_c^3 - \frac{\sqrt{2}}{\sqrt{\pi}} \left[2u^2 + 3\sqrt{2} c_\xi \sigma_c u + 3 c_\xi^2 \sigma_c^2 - 1 \right] \exp(-u^2) \Bigg\} \Bigg\} + P_n \,. \quad (3.22)$$

The parameters setting is same as the aforementioned Brown-Hayne ocean model. Note that both Ice and ocean retrackers are used on-board Jason-2 altimetry mission.

Chapter 4

Areas of study and methodology

In this study, we selected a number of water bodies with different sizes and shapes. The goal is to monitoring the water level variations over time using Jason-2 product. The data can be downloaded directly from Aviso+ satellite altimetry database. Aviso+ is the showcase of CNES activities in altimetry. The website portal opens to hydrology/costal/ice and provides operational and demonstration products. After derived the water level time series using these data, an outlier elimination function is implemented to reject the error measurements. Additionally, a validation with different databases are also carried out in the experiments.

4.1 Study areas

4.1.1 Benue River

The Benue river, previously know as the Chadda River or Tchadda, is the major tributary of the Niger River located in Nigeria. The river is approximately $1400\,\mathrm{m}$ long and is almost entirely navigable during the summer months, which makes it an important transportation route in the neighboring regions. Regarding to the confluence, the mean discharge of Benue River before 1960 was $3400\,\mathrm{m}^3/\mathrm{s}$, that is $900\,\mathrm{m}^3/\mathrm{s}$ larger than Niger River. However, due to irrigation in the recent years, the runoff of Benue reduced significantly. With poor in-situ gauge station coverage, monitoring this river with satellite radar altimetry mission Jason-2 is a feasible solution. Figure 4.1 shows the location of Benue River and the Jason-2 ground track intersects with it, red dot indicate the virtual station location.

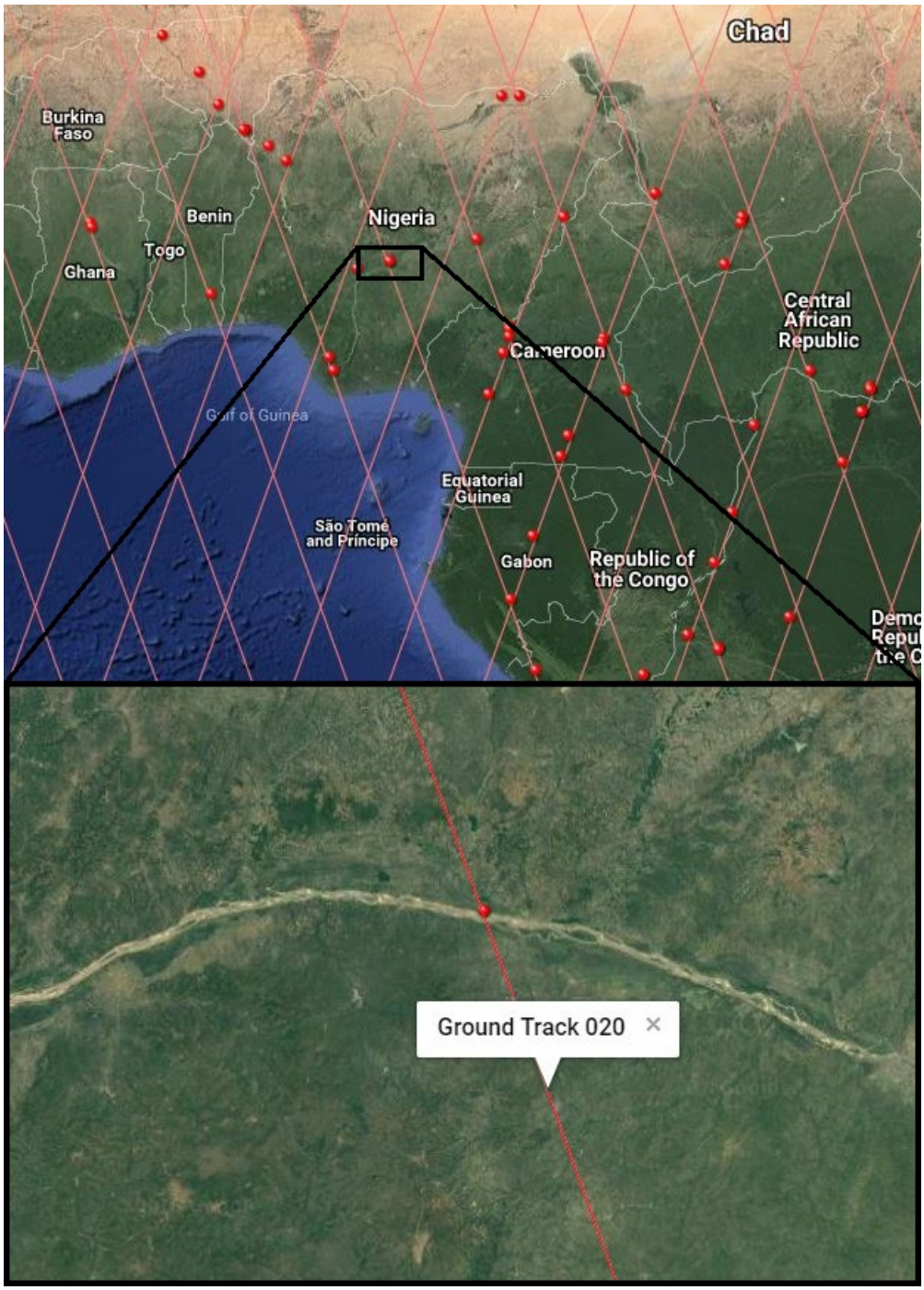

Figure 4.1: *Location of Benue River and intersect Jason-2 ground track*

4.1.2 Tsimlyansk Reservoir

Tsimlyansk reservoir (Figure 4.2) is an artificial lake created by a giant dam at the great band of the Don basin. The reservoir is one of the largest in Russia, providing power and irrigation and the capability of flood control to the Rostov and Volgograd regions. The reservoir also provides an essential waterway between Volga River and the Sea of Azov. Tsimlyansk Reservoir and Don basin are nearly coincide with the Jason-2 ground track 083, which makes it a perfect research object both in spatial and temporal dimensions.

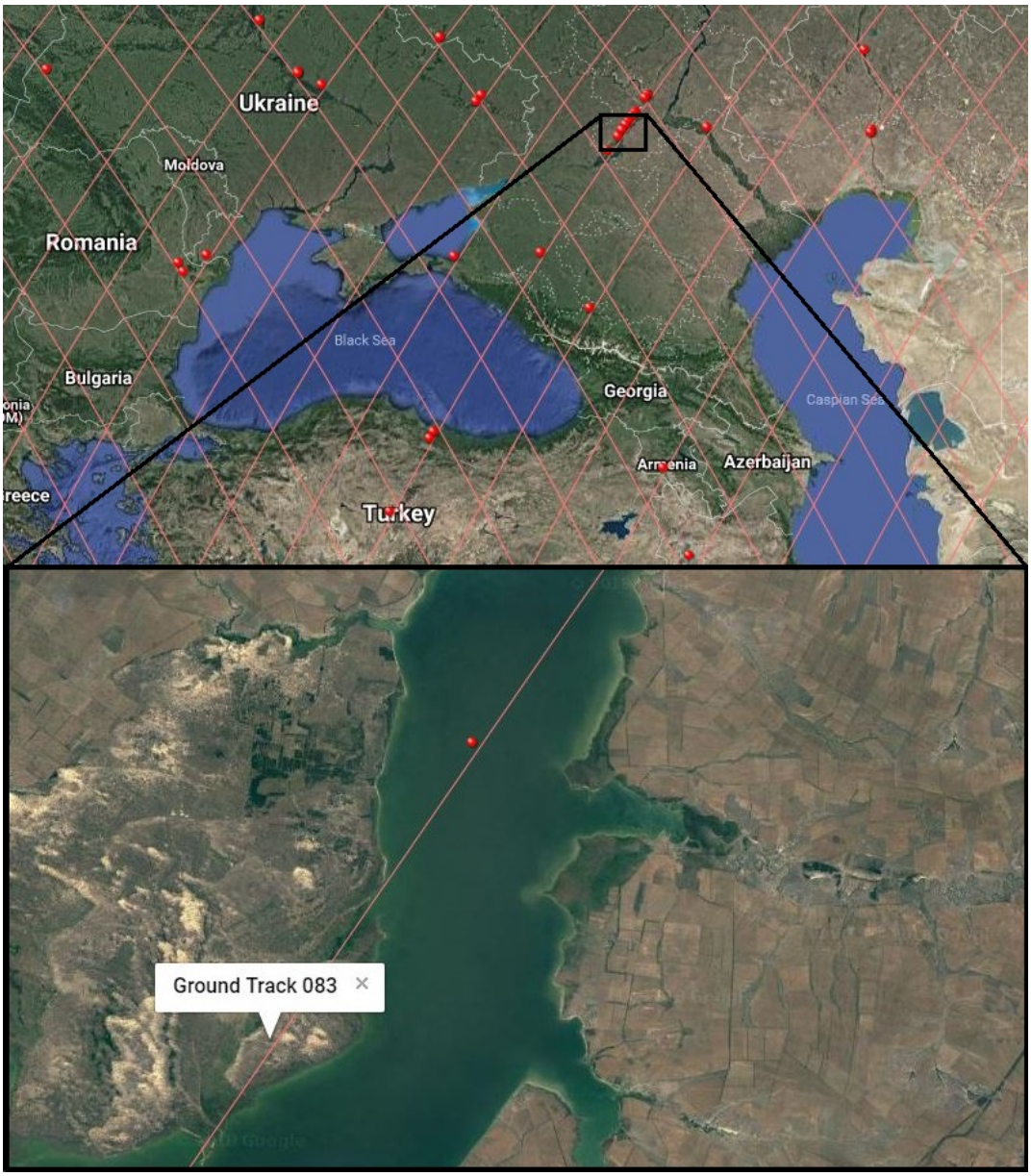

Figure 4.2: *Location of Tsimlyansk Reservoir and intersect Jason-2 ground track*

4.1.3 Amazon River

The Amazon River (Figure 4.3) in South America is the world's largest river with an average discharge about $209\,000\,\mathrm{m}^3/\mathrm{s}$, greater than the next seven largest independent rivers together. The Amazon represents 20% of the global river discharge to the ocean (Moura et al., 2016). With more than one intersection with several satellite altimetery ground tracks and clear water surface, monitoring Amazon River water level variations is a valuable and meaningful task.

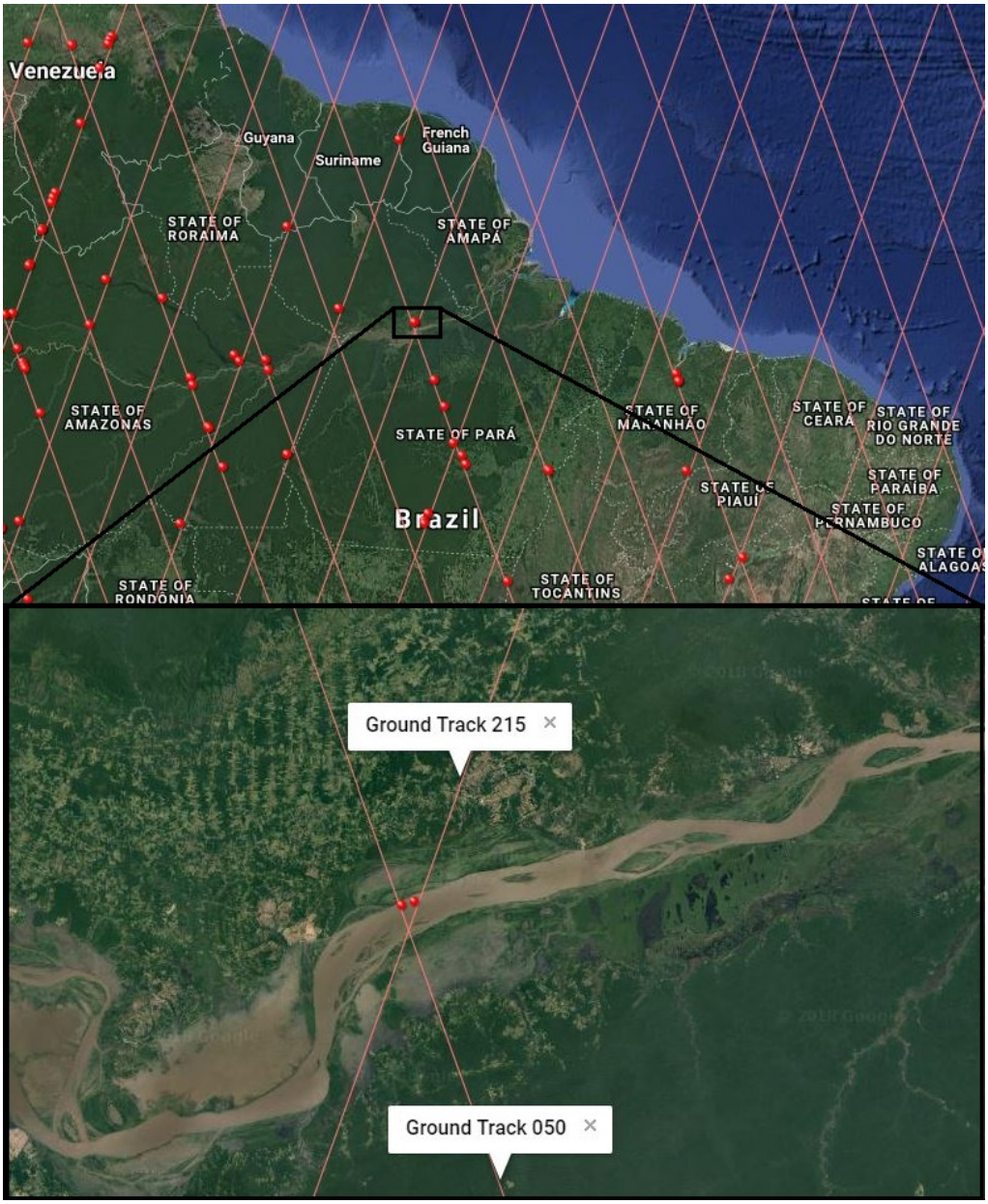

Figure 4.3: *Location of Amazon River and intersect Jason-2 ground track*

4.2 Methodology

4.2.1 Data selection

A virtual station is defined when a satellite ground track intersects with water bodies. Water level variations can therefore be derived each time when satellite flies over the water surface. With less than 10 days of revisit time, Jason-2 provides an fairly high temporal resolution over aforementioned water bodies. In order to get more accurate time series and avoid off-nadir effects, water and land surfaces are suggested to be clearly distinguished. A general method is to generate water mask from satellite imagery and select the point lying on both river mask and satellite ground track as the virtual station.

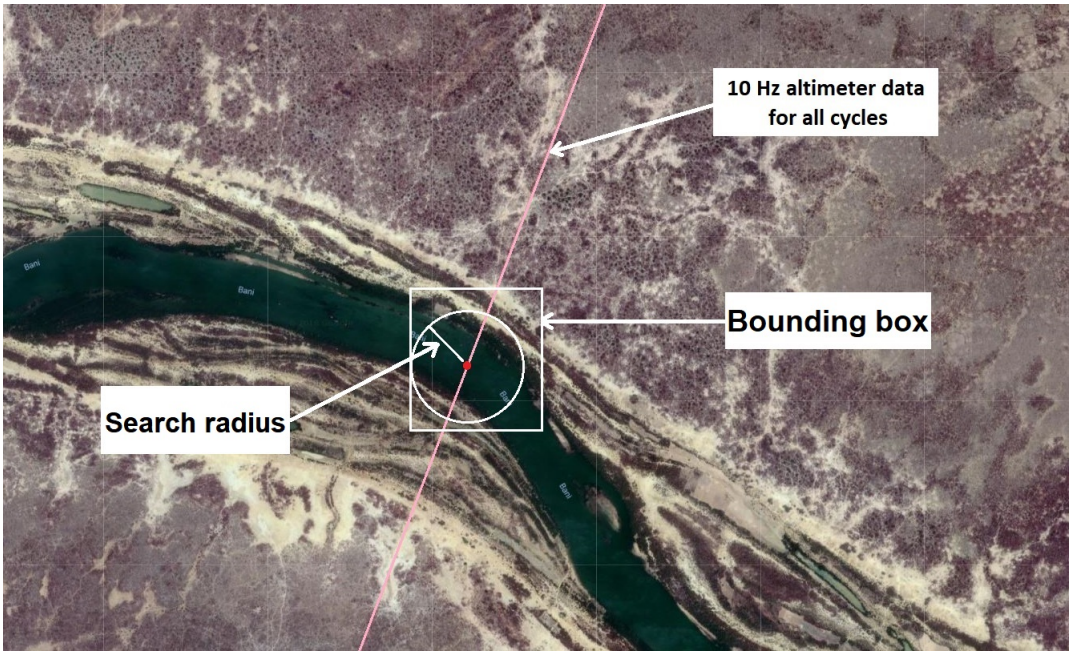

Figure 4.4: *Schematic of selection principle of virtual station, search bounding box and search radius*

In this study, we use the same method to chose the virtual station as Tourian (2013). The coordinate of a virtual station is the intersection point between the central line of the river mask and satellite ground track. A search radius will depend by river width for data retrieve. Because of the large data amount over spatial and temporal domains, the computational cost of the retrieve process might be exponentially high. Therefore, we form a bounding box around the virtual station area to crop unused data and reduce the computing time. The location coordinates of both virtual station and bounding box should be given as input parameters. Figure 4.4 shows the chosen principle of virtual station, search bounding box and search radius schematically. Radar altimetry data within the chosen area are extracted to generate water level time series. This process guarantees that the backscattered waveform is in Brown or quasi-Brown model, for

which the performance of retracking algorithms are the best.

4.2.2 Rejection of outliers

Since the distribution of residuals is typically normal, a data snooping process is implemented on the residual water level. An outliers detection algorithm based on the data snooping method searches for the maximum gross error during the measurements (Tourian, 2013). For the purpose of estimating the water level variations an interannual monthly mean is defined as follow:

$$\bar{H}(t) \;=\; a_0 + a_1(t) + \sum_{i=2}^{3} a_i \cos(\omega_i t) + b_i \sin(\omega_i t)\,, \tag{4.1}$$

where ω is the angular frequency of annual (ω_2) and semi-annual(ω_3) variation. a_0, a_1, a_i and b_i are the unknown coefficients of the model that can be derived using least square estimation. The water level residual is:

$$r(t) \;=\; H(t) - \bar{H}(t)\,. \tag{4.2}$$

By choosing the suitable confidence level α, the critical value $k_{\alpha/2}$ can be derived under the null hypothesis that no outlier is remaining. Here, we chose 95% for α, which means a critical value of 1.96 for normal distribution. Thus, the null hypothesis will be accepted if:

$$-\,k_{\alpha/2} < \frac{r(t)}{\sigma} < k_{\alpha/2}\,, \tag{4.3}$$

where the σ is the standard deviation of the $r(t)$.

4.2.3 Time series generation

Initially, the visual realization of the virtual station and search area location is necessary. The computation of the water level should consider the reference geoid height and several corrections as we described in section 2.2. The basic equation of corrected water level derived from chosen altimetry data according to equation (2.4) reads:

$$\begin{aligned} h \;&=\; H - \left(\hat{R} - \sum_j \Delta R_j\right) \\ &=\; H - \hat{R} + \Delta Ion + \Delta DTC + \Delta WTC + \Delta PT + \Delta ET + h_{\mathrm{G}}\,, \end{aligned} \tag{4.4}$$

in which:

ΔIon = Ionospheric correction ΔDTC = Dry tropospheric correction

ΔWTC = Wet tropospheric correction ΔPT = Pole tide correction

ΔET = Earth tide correction h_{G} = Geoid height

Afterwards, different on-board retracking algorithm is used to correct the water level measurements. For Jason-2 radar altimetry mission, normally the Ice-3 retracker provides the most precise results on Ku-band (Schwatke et al., 2015). Finally, the outliers are rejected and we can obtain the water level time series. The processing pipeline is summarized in Figure 4.5.

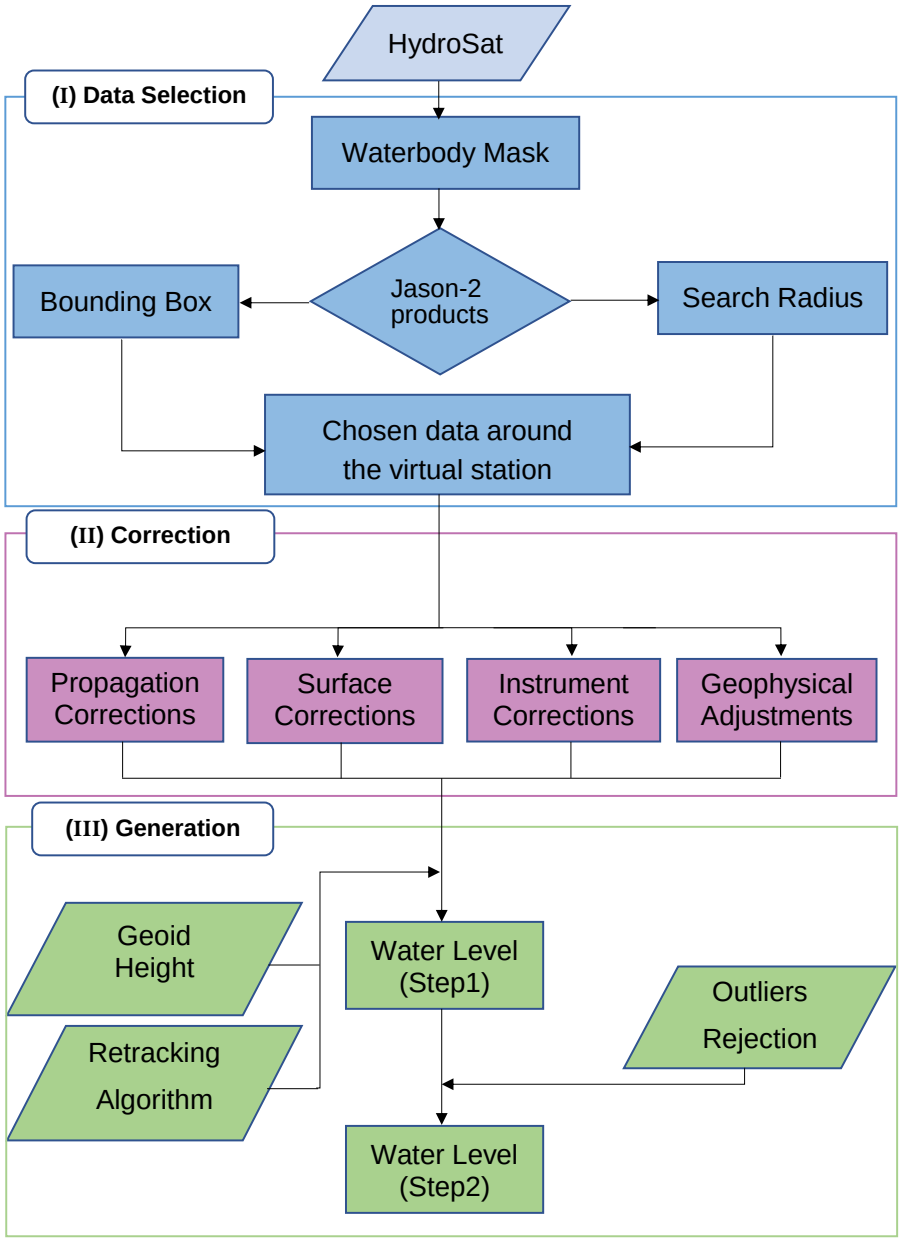

Figure 4.5: *Data processing scheme for time series generation*

4.2.4 Performance metrics

In order to evaluate the biases within the dataset A, the standard deviation (SD) reads:

$$\mathrm{SD} = \sqrt{\frac{\sum_{i=1}^{n}(A_i - \bar{A})^2}{n-1}}. \tag{4.5}$$

For the purpose of comparing the generated time series with results from different databases, various performance metrics can be analyzed. Here, we use correlation coefficient (Corr), root-mean-square error (RMSE) to compare the results.

Correlation coefficient gives the description of the coincide information available between two datasets with a known distribution. For dataset A and dataset B, the correlation coefficient is given as follow:

$$\mathrm{Corr} = \frac{\sum_{i=1}^{n}(A_i - \bar{A})(B_i - \bar{B})}{\sqrt{\sum_{i=1}^{n}(A_i - \bar{A})^2 \sum_{i=1}^{n}(B_i - \bar{B})^2}}. \tag{4.6}$$

In this study, datasets A and B represent the water level time series from different data sources. Moreover, concerning the biases between two datasets A and B, the root-mean-square error should be evaluated as follow:

$$\mathrm{RMSE} = \sqrt{\frac{\sum_{i=1}^{n}(A_i - B_i)^2}{n}}. \tag{4.7}$$

Chapter 5

Experiments and results

In this chapter, we generate the water level variations over the aforementioned water bodies: Benue River, Tsimlyansk Reservoir and Amazon River. Among all the retrackers on-board Jason-2 altimetry mission, we use Ice retracking method, which shows the best performance regarding the water level and standard deviation. The standard deviation of each implementation is also given in the time series and a separate scatter plot. Moreover, due to the insufficient in-situ gauge station over these locations, the validation between the thesis results and DAHITI, Hydroweb databases have been carried out. The data points of the coincide date are compared in terms of the correlation coefficient and RMSE.

One can download Jason-2 products from Aviso+ Data Center (https://www.aviso.altimetry.fr). The satellite tracks was loaded onto Google Earth software via the Aviso pass locater application. Therefore, choosing the feasible virtual station location and their respective track numbers are straightforward with the help of visualization. Table 5.1 shows the details of the chosen virtual station, search window and search radius over different water bodies.

Table 5.1: *Parameters used for data selection*

Object	Track	Virtual Station		Search window		Search radius
		Lat [°]	Lon [°]	Lat [°]	Lon [°]	[m]
Benue	20	8.0002	7.7491	7.9 8.1	7.6 7.9	2000
Tsimlyansk	83	48.0875	42.9487	47.9 48.2	42.7 43.2	5000
Amazon	50	-1.9625	-53.8669	-2.1 −1.8	-54.1 -43.7	5000

The processed time series in Hydroweb (https://hydroweb.theia-land.fr) and DAHITI (https://dahiti.dgfi.tum.de) databases can be directly downloaded for further comparison and validation. To give a graphical intuition of the comparison, the water level time series within the same time frame and scatter plots will be shown in the following section.

5.1 Benue River

For Benue River, the Jason-2 ground track 20 intersects with the river central line at the latitude around $8°$ and longitude around $7.5°$ (Table 5.1). 272 measurements were used to generate the water level time series from 12 July 2008 to 23 September 2016. Figure 5.1 below shows the result of outliers rejection. Among all the observations, the blue ones represent the acceptable data and the red ones are the outliers being eliminated. The distribution of standard deviation mainly located between 0 and 0.25, which shows the commendable capability of retracking algorithm on this dataset.

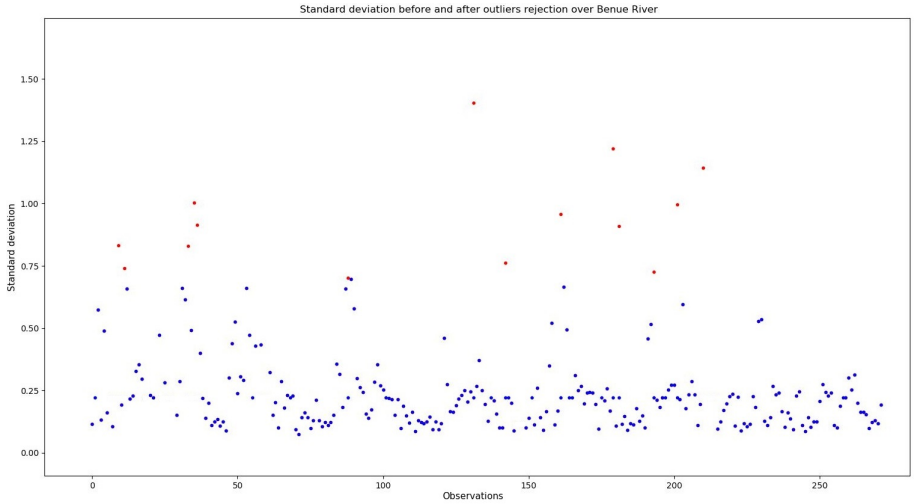

Figure 5.1: *Standard deviation before and after outliers rejection over Benue River*

Figure 5.2 gives the Benue River water level time series. The red bar around each data point shows the standard deviation at the specific time. Notably, the time interval between 2 September 2015 and 17 May 2016 we get a dashed line with no standard deviation bars around it. This is due to the missing data in this period from the database.

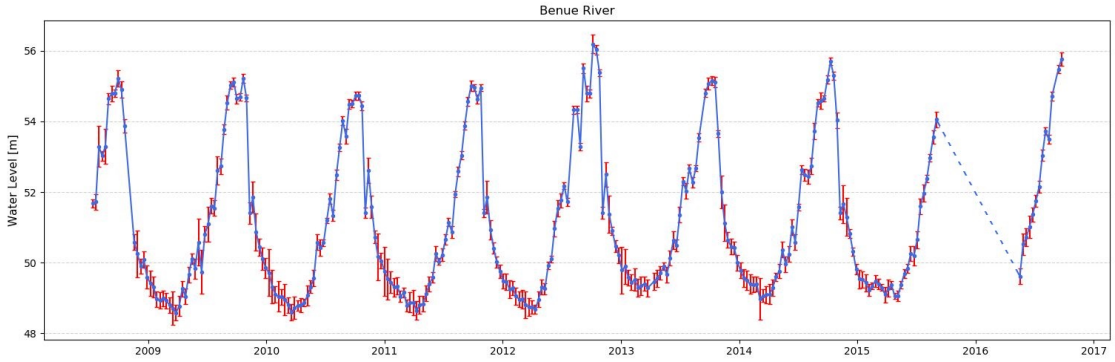

Figure 5.2: *Benue River time series with standard deviation*

Afterwards, within the same period of time, Benue River water level time series of this

study, DAHITI database and Hydroweb database were plotted in a joint way (Figure 5.3). The seasonal and annual variation trends are equal and the water level are almost coincide. Unfortunately, there are still measurement noises that are not eliminated by the developed algorithm.

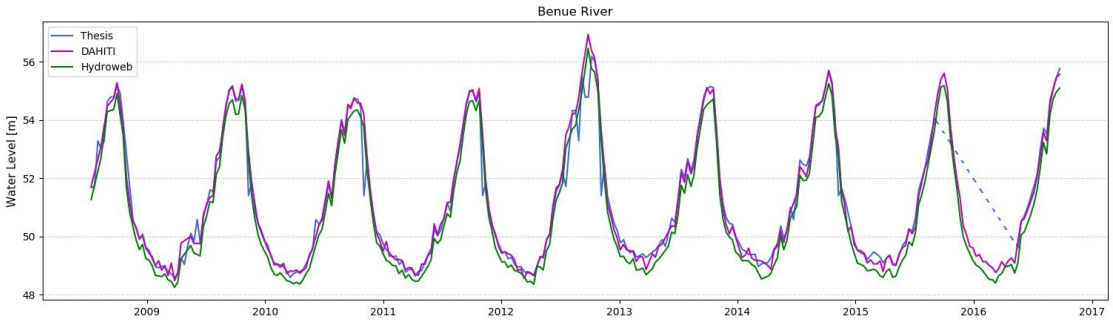

Figure 5.3: *Time series for Benue river from different databases*

The scatter plots for the our time series with respect to other databases are shown in Figure 5.4. We also calculated the performance metrics of our time series compares with DAHITI and Hydroweb databases. The results is shown in Table 5.2, in which the RMSE value represents the root-mean-square error. The comparison between our result and DAHITI database gives a good statistic with a RMSE of $17.1\,\mathrm{cm}$ and correlation coefficient of 0.98. With the correlation of 96%, our result has a RMSE of $32.2\,\mathrm{cm}$ against Hydroweb, which is reasonable according to the height difference shown in Figure 5.3.

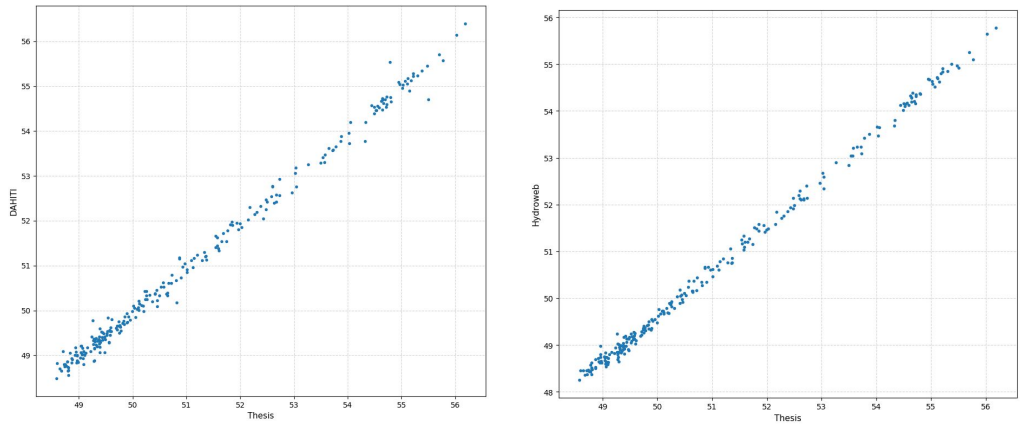

(a) *Thesis vs DAHITI* ***(b)*** *Thesis vs Hydroweb*

Figure 5.4: *Scatter plots for our result against other databases over Benue River*

Table 5.2: *Performance metrics of result of this study compared with DAHITI and Hydroweb over Benue River*

Data source	Correlation coefficient	RMSE [cm]
DAHITI	0.98	17.1
Hydroweb	0.96	32.2

5.2 Tsimlyansk Reservoir

For Tsimlyansk Reservoir, the Jason-2 ground track 83 crosses over the water mask. Here, we choose the virtual station at latitude $48.0875°$ and longitude $42.9487°$ (Table 5.1). 274 measurements were used to generate the water level time series from 15 July 2008 to 25 September 2016. The outliers rejection result Figure 5.5 demonstrates that we encounter greater standard deviations in this time series.

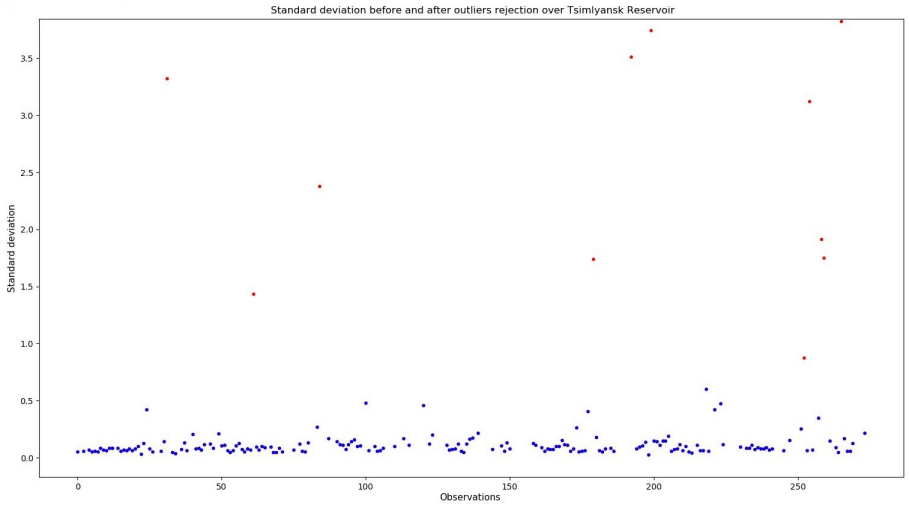

Figure 5.5: *Standard deviation before and after outliers rejection over Tsimlyansk Reservoir*

Next, the Tsimlyansk Reservoir water level time series together with the standard deviation bars are shown in Figure 5.6.

The following Figure 5.7 shows the Tsimlyansk Reservoir water level time series of this study, DAHITI database and Hydroweb database. Interestingly, in the previous Figure 5.6 we found some measurements bounce around along the time series. This might be the consequence of off-nadir effect or mistake in defining the virtual station. However, we noticed that DAHITI database filters out these bounce around measurements with Kalman filtering. This explains why they have straight lines at these time frames. Additionally for Hydroweb, they have much finer temporal resolution after the year of 2015. This is due to the fact that they take account for the data from 10 ground tracks of multiple missions, which would deliver more observations.

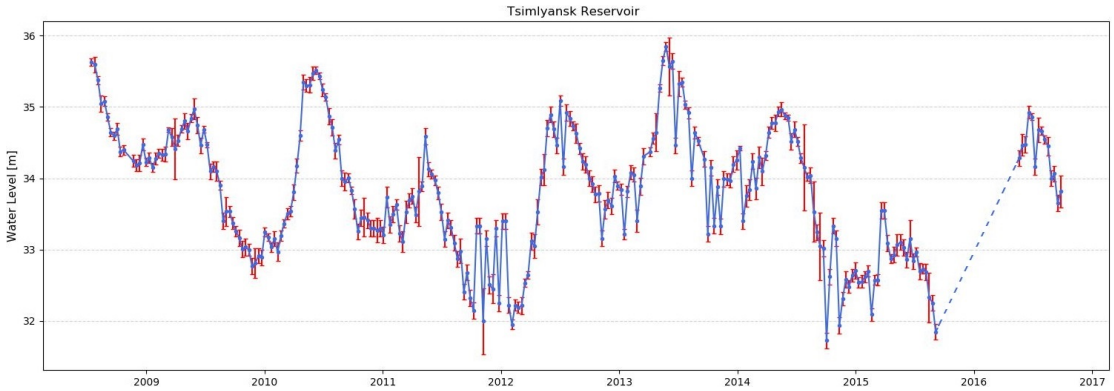

Figure 5.6: *Tsimlyansk Reservoir time series with standard deviation*

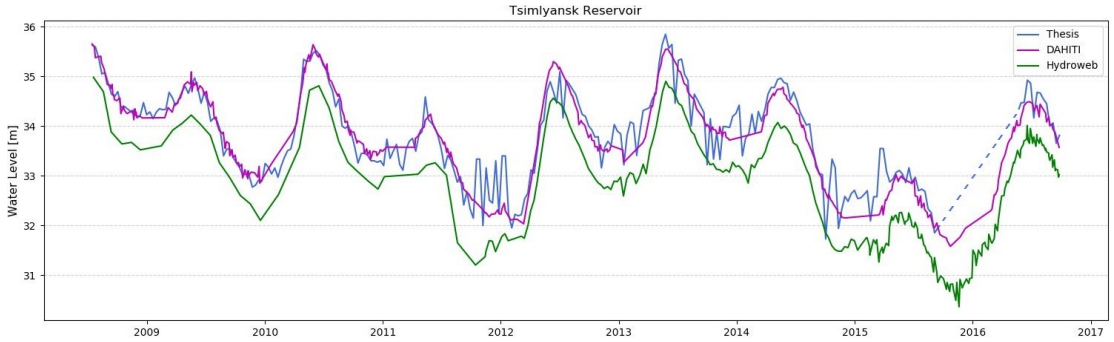

Figure 5.7: *Time series for Tsimlyansk Reservoir from different databases*

Not surprisingly, the difference between the three curves is significantly increased compare to the former case. Even though the trends of water level are the same, the heights give the disagreement. Obviously, our result shows more compromise with DAHITI's time series, although at some part the height difference is not satisfactory. In addition, the average heights different between our result and Hydroweb is more than $0.5\,\mathrm{m}$.

The scatter plots Figure 5.8 also stress the same results. We noticed that the large disagreements are mainly due to our bouncing around measurements. Table 5.3 gives the performance metrics. we figured out the largest difference is between our result and Hydroweb water level at $72.5\,\mathrm{cm}$. Comparing to both external databases, our result have higher correlation coefficient and lower RMSE to the DAHITI time series.

Table 5.3: *Performance metrics of result of this study compared with DAHITI and Hydroweb over Tsimlyansk Reservoir*

Data source	Correlation coefficient	RMSE [cm]
DAHITI	0.86	48.9
Hydroweb	0.83	75.2

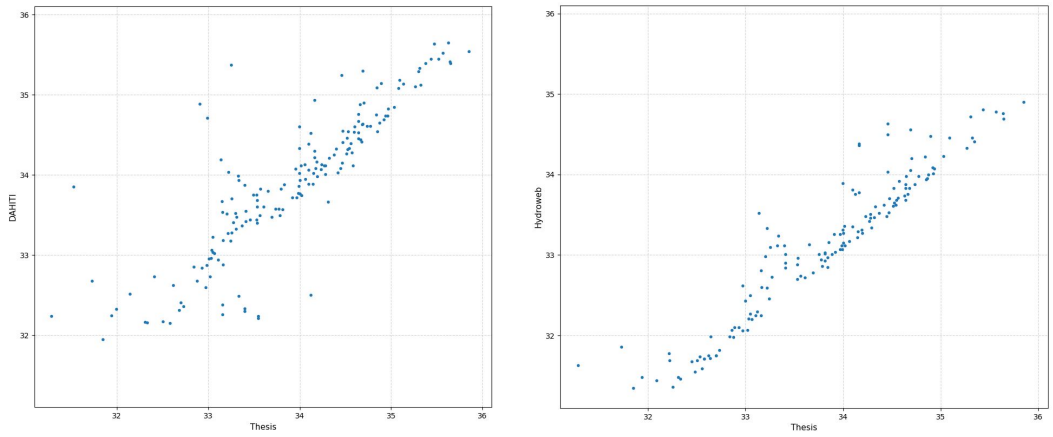

(a) *Thesis vs DAHITI* ***(b)*** *Thesis vs Hydroweb*

Figure 5.8: *Scatter plots for our result against other databases over Tsimlyansk Reservoir*

5.3 Amazon River

For Amazon River, the Jason-2 ground track 50 is used here to generate the water level time series at the latitude $-1.9625°$ and longitude $-53.8669°$ (Table 5.1). Due to the wider width of Amazon River, the search radius for data selection should be larger correspondingly. 272 measurements were used to generate the water level time series from 13 July 2008 to 24 September 2016. The outliers rejection result is shown in Figure 5.9. One obvious phenomenon is that the standard deviations are quite large compare to the former cases. The Amazon River water level time series (Figure 5.10) indicates the same phenomenon. This is mainly due to the large river discharge and rainy weather in Amazon basin. Thus, the water levels change quite often and the monthly average also varies a lot.

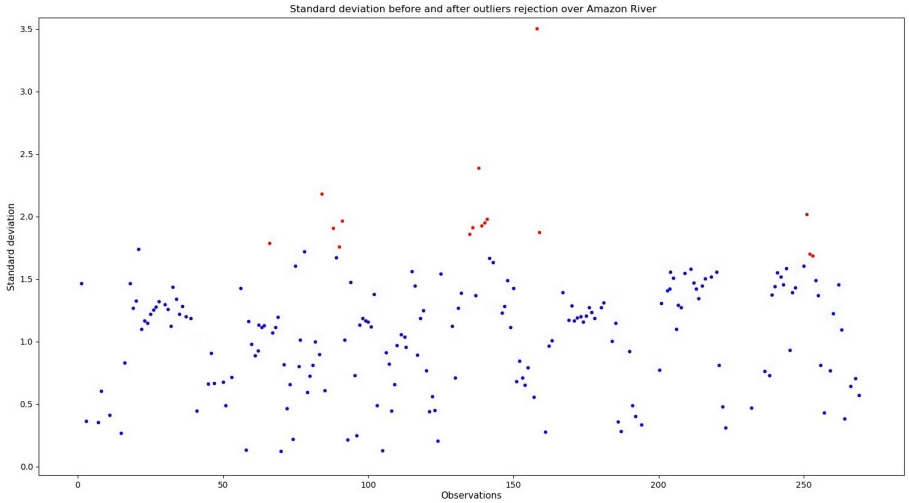

Figure 5.9: *Standard deviation before and after outliers rejection over Amazon River*

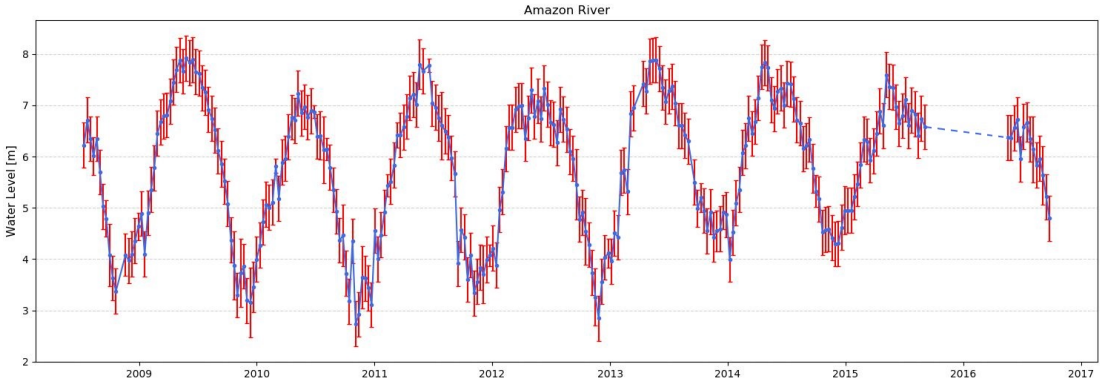

Figure 5.10: *Amazon River time series with standard deviation*

The water level time series at same virtual station location from different data sources are shown in Figure 5.11. The heights and the trends of water level variations are quite similar. It is interesting to notice that the results from our study and Hydroweb database normally have height variations within small time frames but DAHITI does not. This is again because in time series generation of DAHITI, they take advantage of the data filtering technique to reduce and eliminate the noisy measurements. Therefore, their water level time series is smoother compares to the others.

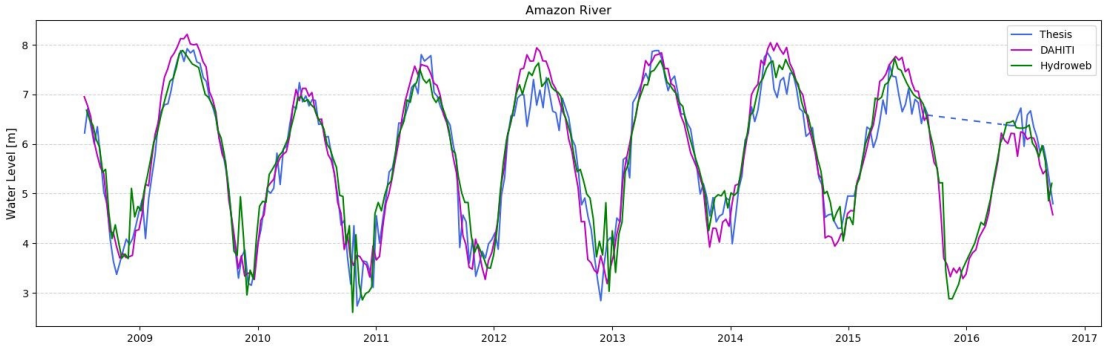

Figure 5.11: *Time series for Amazon River from different databases*

The scatter plots (Figure 5.12) also emphasize the rapid water level variations due to the large river discharge and rainy weather in Amazon River. Table 5.4 gives the performance metrics of our time series compares with DAHITI and Hydroweb databases. Our result achieved an acceptable correlation coefficient on both databases. However, the RMSE is relatively high (more than $30\,\mathrm{cm}$). Recall that in Figure 5.11, the heights varies a lot within small time frames, which could bring a larger RMSE value.

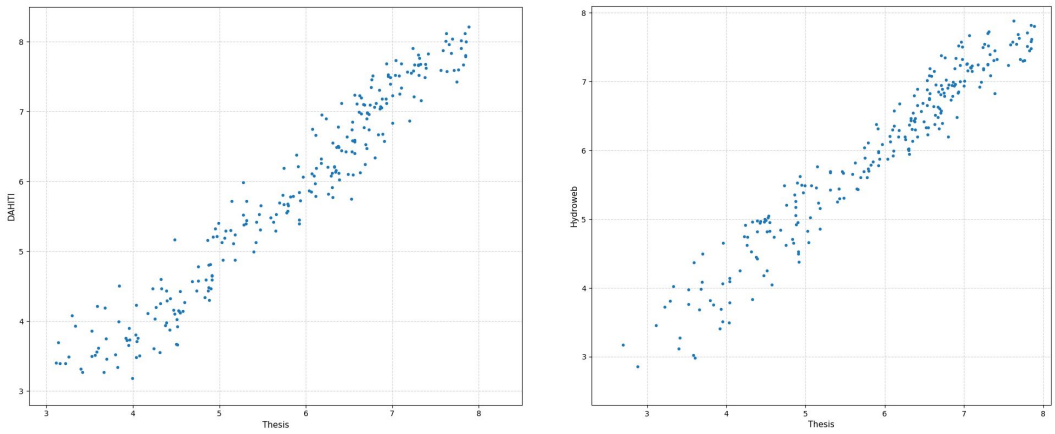

(a) *Thesis vs DAHITI* ***(b)*** *Thesis vs Hydroweb*

Figure 5.12: *Scatter plots for our result against other databases over Amazon River*

Table 5.4: *Performance metrics of result of this study compared with DAHITI and Hydroweb over Amazon River*

Data source	Correlation coefficient	RMSE [cm]
DAHITI	0.95	35.8
Hydroweb	0.93	32.6

Chapter 6

Conclusion and outlook

6.1 Conclusion

An accurate and near real-time water level monitoring is necessary for establishing the hydrologic model in continental-domain. Over small and complex inland water bodies, radar altimeters have shown the capability to give the correct answer. This thesis motivates the monitoring scheme with the help of satellite altimetry missions due to the insufficient in-situ measurements over inland surface water bodies. We have investigated the measurements process in detail regarding to data selection, correction and time series generation. The final water level time series shows acceptable performance in multiple study areas, especially in Benue River case. By comparing the data generated from this study with other providers such as DAHITI and Hydroweb, the precision of water levels are also proved to be feasible and convincible. Furthermore, the differences in spatial and temporal resolutions, applied corrections, retracking methods and post-processing give us a better intuition of how to improve the accuracy for further studies.

Generating reasonable water level time series may face multiple problems. One challenge is how to build flexible and robust error estimation algorithm. A proper algorithm should have the capability to generalize over majority of inland applications. Additionally, an agile outliers rejection function is also needed for correcting the noisy observations in the post-processing stage. One can also using filters, say Kalman filter, to clean out the anomolies within the measurements. It is also worthy to try out different radar altimeter bands over different areas. Moreover, different reference ellipsoids make great height variations. Last but not least, one also needs novel retracking algorithms, which can significantly reduce the erroneous in range estimations.

6.2 Future work

Future work should look at the possibility of improvement the spatial and temporal resolutions with multiple datasets from different satellite altimetry missions. An advanced outliers detection and rejection algorithm could also be helpful for generating accurate

time series. Furthermore, novel retracking methods can help us to fix the noisy range estimations and improve the performance. Finally, for the purpose of viewing our water bodies in different perspectives, the combination of radar altimetry and satellite imagery can also be a solution for monitoring water level variations, water discharge and storage in a joint way.

Bibliography

Abbott M., Bathurst J., Cunge J., O'Connell P., and Rasmussen J. (1986). An introduction to the European Hydrological System — Systeme Hydrologique Europeen, "SHE", 1: History and philosophy of a physically-based, distributed modelling system. Journal of Hydrology, 87 (1): 45 –59. DOI: https://doi.org/10.1016/0022-1694(86)90114-9.

Alsdorf D. E. and Lettenmaier D. P. (2003). Tracking Fresh Water from Space. Science, 301 (5639): 1491–1494. DOI: 10.1126/science.1089802.

Bao L., Lu Y., and Wang Y. (2009). Improved retracking algorithm for oceanic altimeter waveforms. Progress in Natural Science, 19 (2): 195 –203. DOI: 10.1016/j.pnsc.2008.06.017.

Barrick D. E. and Lipa B. J. (1985). Analysis and Interpretation of Altimeter Sea Echo. Satellite Oceanic Remote Sensing, 27: 61 –100. DOI: 10.1016/S0065-2687(08)60403-3.

Berry P. A. M., Garlick J. D., Freeman J. A., and Mathers E. L. (2005). Global inland water monitoring from multi-mission altimetry. Geophysical Research Letters, 32 (16). DOI: 10.1029/2005GL022814.

Berry P., G Smith R., Freeman J., and Benveniste J. (2007). *Near-Real-Time Monitoring of Global Rivers and Lake Heights using EnviSat and Jason-1 Altimeter data*. Tech. rep.

Bevis M., Businger S., Herring T. A., Rocken C., Anthes R. A., and Ware R. H. (1992). GPS meteorology: Remote sensing of atmospheric water vapor using the Global Positioning System. Journal of Geophysical Research: Atmospheres, 97 (D14): 15787–15801.

Biancamaria S., Andreadis K. M., Durand M., Clark E. A., Rodriguez E., Mognard N. M., Alsdorf D. E., Lettenmaier D. P., and Oudin Y. (2010). Preliminary Characterization of SWOT Hydrology Error Budget and Global Capabilities. IEEE Journal of Selected Topics in Applied Earth Observations and Remote Sensing, 3 (1): 6–19. DOI: 10.1109/JSTARS.2009.2034614.

Birkett C. M., Mertes L. A. K., Dunne T., Costa M. H., and Jasinski M. J. (2002). Surface water dynamics in the Amazon Basin: Application of satellite radar altimetry. Journal of Geophysical Research: Atmospheres, 107 (D20): LBA 26–1–LBA 26–21. DOI: 10.1029/2001JD000609.

Brown G. (1977). The average impulse response of a rough surface and its applications. IEEE Transactions on Antennas and Propagation, 25 (1): 67–74. DOI: 10.1109/TAP.1977.1141536.

Calmant S., Seyler F., and Cretaux J. F. (2008). Monitoring Continental Surface Waters by Satellite Altimetry. Surveys in Geophysics, 29 (4): 247–269. DOI: 10.1007/s10712-008-9051-1.

Calmant S. and Seyler F. (2006). Continental surface waters from satellite altimetry. Comptes Rendus Geoscience - C R GEOSCI, 338: 1113–1122.

Cartwright D. E. and Edden A. C. (1973). Corrected Tables of Tidal Harmonics. Geophysical Journal of the Royal Astronomical Society, 33 (3): 253–264. DOI: 10.1111/j.1365-246X.1973.tb03420.x.

Cartwright D. E. and Tayler R. J. (1971). New Computations of the Tide-generating Potential. Geophysical Journal International, 23 (1): 45–73. DOI: 10.1111/j.1365-246X.1971.tb01803.x.

Cazenave A., Bonnefond P., Dominh K., and Schaeffer P. (1997). Caspian sea level from Topex-Poseidon altimetry: Level now falling. Geophysical Research Letters, 24 (8): 881–884. DOI: 10.1029/97GL00809.

Chelton D. B., Ries J. C., Haines B. J., Fu L.-L., and Callahan P. S. (2001). Chapter 1 Satellite Altimetry. International Geophysics, 69. Ed. by L.-L. Fu and A. Cazenave: 1 –ii. DOI: 10.1016/S0074-6142(01)80146-7.

CNES and CLS (2014). *The Centre national d'études spatiales*. URL: https://cnes.fr/en.

Crétaux J.-F. and Birkett C. (2006). Lake studies from satellite radar altimetry. Comptes Rendus Geoscience, 338 (14). La Terre observée depuis l'espace: 1098 –1112. DOI: 10.1016/j.crte.2006.08.002.

Da Silva J. S., Calmant S., Seyler F., Filho O. C. R., Cochonneau G., and Mansur W. J. (2010). Water levels in the Amazon basin derived from the ERS 2 and ENVISAT radar altimetry missions. Remote Sensing of Environment, 114 (10): 2160 –2181. DOI: 10.1016/j.rse.2010.04.020.

Davis C. H. (1995). Growth of the Greenland ice sheet: a performance assessment of altimeter retracking algorithms. IEEE Transactions on Geoscience and Remote Sensing, 33 (5): 1108–1116. DOI: 10.1109/36.469474.

Davis C. H. (1997). A robust threshold retracking algorithm for measuring ice-sheet surface elevation change from satellite radar altimeters. IEEE Transactions on Geoscience and Remote Sensing, 35 (4): 974–979. DOI: 10.1109/36.602540.

Davis J., Herring T., Shapiro I., Rogers A., and Elgered G. (1985). Geodesy by radio interferometry: Effects of atmospheric modeling errors on estimates of baseline length. Radio science, 20 (6): 1593–1607.

Deng X. and Featherstone W. E. (2006). A coastal retracking system for satellite radar altimeter waveforms: Application to ERS-2 around Australia. Journal of Geophysical Research: Oceans, 111 (C6). DOI: 10.1029/2005JC003039.

Deng X. (2003). "Improvement of Geodetic Parameter Estimation in Coastal Regions from Satellite Radar Altimetry". PhD thesis. Curtin University of Technology.

Desai S. D. (2002). Observing the pole tide with satellite altimetry. Journal of Geophysical Research: Oceans, 107 (C11): 7–1–7–13. DOI: 10.1029/2001JC001224.

Desportes C., Obligis E., and Eymard L. (2007). On the wet tropospheric correction for altimetry in coastal regions. IEEE transactions on geoscience and remote sensing, 45 (7): 2139–2149.

Dubey A. K., Gupta P., Dutta S., and Singh R. P. (2015). Water Level Retrieval Using SARAL/AltiKa Observations in the Braided Brahmaputra River, Eastern India. Marine Geodesy, 38 (sup1): 549–567. DOI: 10.1080/01490419.2015.1008156.

Dudley B. Chelton J. C. R. and Haines B. J. (2001). "Satellite Altimetry and Earth Sciences: A Handbook of Techniques and Applications". In: ed. by L. Fu and A. Cazenave. Elsevier Science. Chap. Satellite Altimetry, pp. 1–132.

Fenoglio-Marc L., Dinardo S., Scharroo R., Roland A., Sikiric M. D., Lucas B., Becker M., Benveniste J., and Weiss R. (2015). The German Bight: A validation of CryoSat-2 altimeter data in SAR mode. Advances in Space Research, 55 (11): 2641 –2656. DOI: 10.1016/j.asr.2015.02.014.

Fok H. S. (2012). "Ocean Tides Modeling using Satellite Altimetry". PhD thesis. The Ohio State University.

Frappart F., Minh K. D., L'Hermitte J., Cazenave A., Ramillien G., Le Toan T., and Mognard-Campbell N. (2006a). Water volume change in the lower Mekong from satellite altimetry and imagery data. Geophysical Journal International, 167 (2): 570–584. DOI: 10.1111/j.1365-246X.2006.03184.x.

Frappart F., Calmant S., Cauhopé M., Seyler F., and Cazenave A. (2006b). Preliminary results of ENVISAT RA-2-derived water levels validation over the Amazon basin. Remote Sensing of Environment, 100 (2): 252 –264. DOI: 10.1016/j.rse.2005.10.027.

Gaspar P., Ogor F., Traon P. L., and Zanife O. (1994). Estimating the sea state bias of the TOPEX and POSEIDON altimeters from crossover differences. Journal of Geophysical Research: Oceans, 99 (C12): 24981–24994. DOI: 10.1029/94JC01430.

Getirana A. C. V. and Peters-Lidard C. (2013). Estimating water discharge from large radar altimetry datasets. Hydrology and Earth System Sciences, 17 (3): 923–933. DOI: 10.5194/hess-17-923-2013.

Gommenginger C., Thibaut P., Fenoglio L., Quartly G., Deng X., Gomez-Enri J., Challenor P., and Gao Y. (2011). "Coastal Altimetry". In: pp. 61–101.

GRDC (2018). *Global Runoff Data Centre*. URL: https://www.bafg.de/GRDC/EN/Home/homepage_node.html.

Guo J., Chang X., Gao Y., Sun J., and Hwang C. (2009). Lake Level Variations Monitored With Satellite Altimetry Waveform Retracking. IEEE Journal of Selected Topics in Applied Earth Observations and Remote Sensing, 2 (2): 80–86. DOI: 10.1109/JSTARS.2009.2021673.

Harvey K. D. and Grabs W. (2003). *WMO Report of the GCOS/GTOS/HWRP expert meeting on hydrological data for global studies*. Tech. rep. No. 1156. Toronto, Canada: Report GCOS 84, Report GTOS 32, World Meteorological Organization (WMO)/TD.

Hayne G. (1980). Radar altimeter mean return waveforms from near-normal-incidence ocean surface scattering. IEEE Transactions on Antennas and Propagation, 28 (5): 687–692. DOI: 10.1109/TAP.1980.1142398.

Kashid S. G. and Pardeshi S. A. (2014). A survey of water distribution system and new approach to intelligent water distribution system. 2014 First International Conference on Networks Soft Computing (ICNSC2014): 339–344. DOI: 10.1109/CNSC.2014.6906645.

Kleinherenbrink M., Ditmar P., and Lindenbergh R. (2014). Retracking Cryosat data in the SARIn mode and robust lake level extraction. Remote Sensing of Environment, 152: 38 –50. DOI: 10.1016/j.rse.2014.05.014.

Koblinsky C. J., Clarke R. T., Brenner A. C., and Frey H. (1993). Measurement of river level variations with satellite altimetry. Water Resources Research, 29 (6): 1839–1848. DOI: 10.1029/93WR00542.

Kouba J. (2008). Implementation and testing of the gridded Vienna Mapping Function 1 (VMF1). Journal of Geodesy, 82 (4-5): 193–205.

Kouraev A. V., Zakharova E. A., Samain O., Mognard N. M., and Cazenave A. (2004). Ob' river discharge from TOPEX/Poseidon satellite altimetry (1992–2002). Remote Sensing of Environment, 93 (1): 238 –245. DOI: 10.1016/j.rse.2004.07.007.

Legrésy B. and Remy F. (1997). Altimetric observations of surface characteristics of the Antarctic ice sheet. Journal of Glaciology, 43 (144): 265–275.

Leon J., Calmant S., Seyler F., Bonnet M.-P., Cauhopé M., Frappart F., Filizola N., and Fraizy P. (2006). Rating curves and estimation of average water depth at the upper Negro River based on satellite altimeter data and modeled discharges. Journal of Hydrology, 328 (3). The ICWRER - Symposium in Dresden, Germany: 481 –496. DOI: 10.1016/j.jhydrol.2005.12.006.

Maheu C., Cazenave A., and Mechoso C. R. (2003). Water level fluctuations in the Plata Basin (South America) from Topex/Poseidon Satellite Altimetry. Geophysical Research Letters, 30 (3). DOI: 10.1029/2002GL016033.

Martin T. V., Zwally H. J., Brenner A. C., and Bindschadler R. A. (1983). Analysis and retracking of continental ice sheet radar altimeter waveforms. Journal of Geophysical Research: Oceans, 88 (C3): 1608–1616. DOI: 10.1029/JC088iC03p01608.

MENDES V. (1999). "Modeling the Neutral-Atmosphere Propagation Delay in Radiometric Space Techniques. 353 f". PhD thesis. Universidade de New Brunswick, Fredericton, Canada.

Moura R. L., Amado-Filho G. M., Moraes F. C., Brasileiro P. S., Salomon P. S., Mahiques M. M., Bastos A. C., Almeida M. G., Silva J. M., Araujo B. F., Brito F. P., Rangel T. P., Oliveira B. C. V., Bahia R. G., Paranhos R. P., Dias R. J. S., Siegle E., Figueiredo A. G., Pereira R. C., Leal C. V., Hajdu E., Asp N. E., Gregoracci G. B., Neumann-Leitão S., Yager P. L., Francini-Filho R. B., Fróes A., Campeão M., Silva B. S., Moreira A. P. B., Oliveira L., Soares A. C., Araujo L., Oliveira N. L., Teixeira J. B., Valle R. A. B., Thompson C. C., Rezende C. E., and Thompson F. L. (2016). An extensive

reef system at the Amazon River mouth. Science Advances, 2 (4). DOI: 10.1126/sciadv.1501252.

Munk W. H. and MacDonald G. J. F. (1961). The Rotation of the Earth: A geophysical discussion. Science, 134 (3491): 1683–1684. DOI: 10.1126/science.134.3491.1683-a.

NOAA (2017). OSTM/Jason-2 Products Handbook. National Centers for Environmental information: National Oceanic and Atmospheric Administration.

Obligis E., Desportes C., Eymard L., Fernandes M., Lázaro C., and Nunes A. (2011). "Tropospheric corrections for coastal altimetry". In: *Coastal altimetry*. Springer, pp. 147–176.

Papa F., Durand F., Rossow W. B., Rahman A., and Bala S. K. (2010). Satellite altimeter-derived monthly discharge of the Ganga-Brahmaputra River and its seasonal to interannual variations from 1993 to 2008. Journal of Geophysical Research: Oceans, 115 (C12). DOI: 10.1029/2009JC006075.

Rapley C. G, Laboratory M. S. S., and Agency E. S. (1987). An exploratory study of inland water and land altimetry using Seasat data : Final report. European Space Agency.

Ray R. D. (1999). *A Global Ocean Tide Model From TOPEX/POSEIDON Altimetry: GOT99.2*. Tech. rep. Greenbelt, MD United States: NASA Goddard Space Flight Center.

Rodríguez E., Kim Y., and Martin J. M. (1992). The effect of small-wave modulation on the electromagnetic bias. Journal of Geophysical Research: Oceans, 97 (C2): 2379–2389. DOI: 10.1029/91JC02511.

Roohi S. (2017). "Performance evaluation of different satellite radar altimetry missions for monitoring inland water bodies". PhD thesis. University of Stuttgart.

Rush C (1986). Ionospheric radio propagation models and predictions–A mini-review. IEEE transactions on antennas and propagation, 34 (9): 1163–1170.

Scharroo R, Lillibridge J., Smith W., and Schrama E. (2004). Cross-calibration and long-term monitoring of the microwave radiometers of ERS, TOPEX, GFO, Jason, and Envisat. Marine Geodesy, 27 (1-2): 279–297.

Scharroo R. and Lillibridge J. (2005). Non-Parametric sea-state bias models and their relevance to sea level change studies.

Schreiner W. S., Markin R. E., and Born G. H. (1997). Correction of single frequency altimeter measurements for ionosphere delay. IEEE transactions on geoscience and remote sensing, 35 (2): 271–277.

Schwatke C., Dettmering D., Bosch W., and Seitz F. (2015). DAHITI: an innovative approach for estimating water level time series over inland waters using multi-mission satellite altimetry. Hydrology and Earth System Sciences, 19 (10): 4345–4364. DOI: 10.5194/hess-19-4345-2015.

Shiklomanov A. I., Lammers R. B., and Vörösmarty C. J. (2011). Widespread decline in hydrological monitoring threatens Pan-Arctic Research. Eos, Transactions American Geophysical Union, 83 (2): 13–17. DOI: 10.1029/2002EO000007.

Stefano Vignudelli Andrey G. Kostianoy P. C. and Benveniste J. (2011). Coastal Altimetry. Springer-Verlag Berlin Heidelberg. DOI: 10.1007/978-3-642-12796-0.

Tourian M. J. (2013). "Application of spaceborne geodetic sensors for hydrology". PhD thesis. Geodätisches Institut der Universität Stuttgart.

Tran N., Vandemark D., Labroue S., Feng H., Chapron B., Tolman H. L., Lambin J., and Picot N. (2010). Sea state bias in altimeter sea level estimates determined by combining wave model and satellite data. Journal of Geophysical Research: Oceans, 115 (C3). DOI: 10.1029/2009JC005534.

Tseng K.-H., Shum C., Yi Y., Fok H. S., Kuo C., Lee H., Cheng X., and Wang X. (2013). Envisat Altimetry Radar Waveform Retracking of Quasi-Specular Echoes over the Ice-Covered Qinghai Lake. Terrestrial Atmospheric and Oceanic Sciences, 24: 615–627.

Wahr J. M. (1985). Deformation induced by polar motion. Journal of Geophysical Research: Solid Earth, 90 (B11): 9363–9368. DOI: 10.1029/JB090iB11p09363.

Wingham D., Rapley C., and Griffiths H (1986). New techniques in satellite altimeter tracking systems. 86: 1339–1344.

Wunsch C. (1972). Bermuda sea level in relation to tides, weather, and baroclinic fluctuations. Reviews of Geophysics, 10 (1): 1–49. DOI: 10.1029/RG010i001p00001.